environmental microbiology

Environmental Microbiology (2015) **17**(7), 2542–2556 doi:10.1111/1462-2920.12752

Heavy water and ^{15}N labelling with NanoSIMS analysis reveals growth rate-dependent metabolic heterogeneity in chemostats

Sebastian H. Kopf,[1,2,3*] Shawn E. McGlynn,[1] Abigail Green-Saxena,[2] Yunbin Guan,[1,3] Dianne K. Newman[1,2,3***] and Victoria J. Orphan[1****]**

[1]*Division of Geological and Planetary Sciences, California Institute of Technology, Pasadena, CA, USA.*

[2]*Division of Biology and Biological Engineering, California Institute of Technology, Pasadena, CA, USA.*

[3]*Howard Hughes Medical Institute, California Institute of Technology, Pasadena, CA, USA.*

Summary

To measure single-cell microbial activity and substrate utilization patterns in environmental systems, we employ a new technique using stable isotope labelling of microbial populations with heavy water (a passive tracer) and ^{15}N ammonium in combination with multi-isotope imaging mass spectrometry. We demonstrate simultaneous NanoSIMS analysis of hydrogen, carbon and nitrogen at high spatial and mass resolution, and report calibration data linking single-cell isotopic compositions to the corresponding bulk isotopic equivalents for *Pseudomonas aeruginosa* and *Staphylococcus aureus*. Our results show that heavy water is capable of quantifying *in situ* single-cell microbial activities ranging from generational time scales of minutes to years, with only light isotopic incorporation (~0.1 atom % ^{2}H). Applying this approach to study the rates of fatty acid biosynthesis by single cells of *S. aureus* growing at different rates in chemostat culture (~6 h, 1 day and 2 week generation times), we observe the greatest anabolic activity diversity in the slowest growing populations. By using heavy water to constrain cellular growth activity, we can further infer the relative contributions of ammonium versus amino acid assimilation to the cellular nitrogen pool. The approach described here can be applied to disentangle individual cell activities even in nutritionally complex environments.

Received 5 September, 2014; revised 11 December, 2014; accepted 12 December, 2014. For correspondence. *E-mail sebastian.kopf@colorado.edu; Tel. 609-258-2489; Fax 609-258-5275. **E-mail yunbin@gps.caltech.edu; Tel. 626-395-6874; Fax 626-568-0935. ***E-mail dkn@caltech.edu; Tel. 626-395-3543; Fax 626-395-4135. *****E-mail vorphan@gps.caltech.edu; Tel. 626-395-1786; Fax 626-568-0935.

Introduction

A fundamental challenge in environmental microbiology is discerning what microorganisms are doing in diverse habitats. Being able to answer this question quantitatively is an even more elusive goal, yet necessary to predict the effects of microbial activity on environmental processes. Today it is well recognized that microbial communities are diverse; often it is necessary to parse them at the single-cell level in order to understand how heterogeneous populations operate. Though it is possible to gain valuable insights from measuring microbial activities in bulk, without single-cell resolution, important features of population biology may be missed. Particularly for individual cells, net anabolic activity for growth and maintenance is a key physiological parameter that reflects use of all available resources, and allows specific activities – such as substrate use – to be properly contextualized. Traditional techniques involving isotopically enriched substrates (e.g. with ^{13}C, ^{15}N, ^{34}S, etc.) have the potential to provide such insight, if their utilization at the single-cell level can be measured in combination with that of a universal tracer for general cellular activity.

Multi-isotope secondary ion imaging mass spectrometry (MIMS or NanoSIMS) provides one of the most sensitive and precise analytical methods available to study elemental and isotopic composition at high spatial resolution. This technique has been broadly applied in the field of microbial ecology to study the spatiometabolic activity of diverse microbial communities (Popa *et al.*, 2007; Musat *et al.*, 2008; Dekas *et al.*, 2009; Orphan *et al.*, 2009; Morono *et al.*, 2011; Woebken *et al.*, 2012), soil microbe–mineral colocalization (Herrmann *et al.*, 2006) and symbiotic interactions (Lechene *et al.*, 2007; Foster *et al.*, 2011; Pernice *et al.*, 2012; Thompson *et al.*, 2012) using various ^{15}N labelled isotope tracers. The non-toxic nature of stable isotope labels combined with the high sensitivity and spatial resolution of NanoSIMS has great potential to quantitatively study metabolic processes even

within model organisms ranging from microbes to humans (Steinhauser and Lechene, 2013). Examples include the application of isotopically labelled ^{15}N-thymidine to trace stem cell division and nuclear metabolism in mice (Gormanns *et al*., 2012; Steinhauser *et al*., 2012), ^{13}C-oleic acid to study fatty acid transport in lipid droplets, ^{15}N-leucine to trace protein renewal in kidney cells (Lechene *et al*., 2006), various ^{15}N-labelled amino acids to study protein turnover in hair cell stereocilia (Zhang *et al*., 2012), ^{18}O-trehalose penetration into the nucleus of mouse sperm (Lechene *et al*., 2012), dual ^{13}C and ^{15}N-labelled substrate in microbial activity studies of oral biofilms (Spormann *et al*., 2008) and the utilization of host-derived substrates by intestinal microbiota (Berry *et al*., 2013). As evidenced by this accelerating body of work, secondary ion mass spectrometry (SIMS) increasingly finds application in disciplines as diverse as geobiology, biogeochemistry, host–microbe interactions and biomedical research (see Orphan and House, 2009; Wagner, 2009; Hoppe *et al*., 2013; Steinhauser and Lechene, 2013 for recent reviews). However, many of these disciplines frequently address questions in nutritionally complex environments where substrate-specific ^{13}C- and ^{15}N-based isotopic tracers often capture only a subset of the microbial population.

To overcome the limitations of substrate-specific isotope labels, heavy water (^2H_2O) was recently shown to be a powerful new tracer in environmental systems due to its advantages as a chemically and nutritionally passive isotopic label, and its potential for combined application with other enriched substrates (Kellermann *et al*., 2012; Wegener *et al*., 2012). Heavy water constitutes a general isotopic tracer because it is utilized by all organisms and provides a unique tool for measuring microbial activity in a diverse range of environments. This is particularly useful in complex systems with slow-growing organisms, numerous carbon and nitrogen sources, and diverse heterotrophic populations, because the introduction of substrate-specific tracers can disturb the concentration and availability of autochthonous nutrients and inflate or bias species-specific measures of activity. In contrast, heavy water is easy to administer both in environmental and medical contexts, does not distort substrate availability to the benefit of some organisms over others and is stably incorporated during metabolism into fatty acids and other cellular components with stable C–H bonds (and transiently into exchangeable hydrogen bonds). Additionally, the low natural abundance of ^{2}H (de Laeter *et al*., 2003) enables relatively small isotopic spikes to capture a wide range of microbial activity (hours to months) in a short time span, with higher tracer concentrations enabling detection even of slow environmental populations with generation times of tens to hundreds of years (Hoehler and Jørgensen, 2013). Figure 1 illustrates an example of the theoretically estimated minimal incubation times required to achieve a fatty acid enrichment signal of δ^2H = 5500‰ (or $^{2H}F = 0.1$ at%) with different ^2H_2O isotopic spikes for a wide range of microbial populations doubling over the course of an hour to 100 years (see Appendix S7 for details).

Despite the potential of ^2H_2O as a tracer for microbial activity in environmental microbiology, its application in multi-tracer NanoSIMS studies has been fundamentally limited by the typical limitations in dynamic mass range encountered in multi-collector SIMS instruments. The CAMECA NanoSIMS 50L, for example, is a widely used multicollector secondary ion mass spectrometer equipped with seven electron multiplier detectors or faraday cups that provide simultaneous detection of up to seven masses at a fixed magnetic field strength. SIMS is a

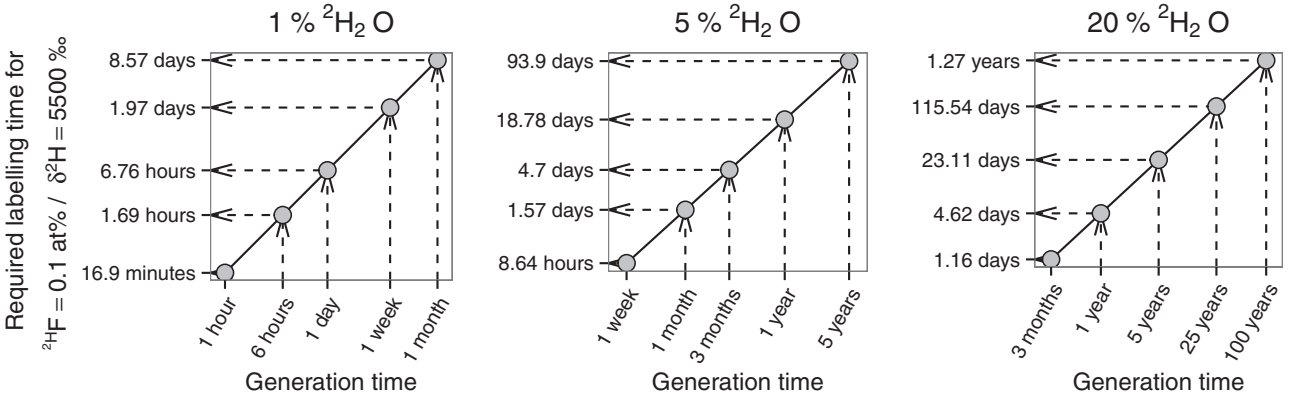

Fig. 1. Incubation time requirements. This figure illustrates the theoretically estimated minimal incubation times required to reach an isotopic enrichment in fatty acid deuterium of $^{2H}F = 0.1$ at% or δ^2H = 5500‰ (in starting material with natural abundance H isotope composition reflecting the international standard mean ocean water, VSMOW), depending on the strength of the isotopic ^2H_2O label and the average generation time of a microbial population. Labelling concentrations above 20% ^2H_2O are not recommended, due to the potential toxic effect on solvent properties and enzyme kinetics (see discussion below, *Important constraints on the quantitative use of ^2H_2O labels* for details).

destructive technique that uses a primary ion beam to gradually ablate the analytical target and generate secondary ions. The destructive nature of SIMS can be particularly problematic in the analysis of organic targets that can be sputtered away quickly and are sometimes in short supply. The parallel detection of all ions of interest is thus an important feature of the NanoSIMS 50L, and its large magnet and multi-collection assemblage typically allow parallel detection of ions with vastly different mass to charge $\left(\frac{m}{z}\right)$ ratios up to ~22:1 (i.e. the maximum $\frac{m}{z}$ can be 22 times larger than the lowest mass: $\left(\frac{m}{z}\right)_{max} = 22 \cdot \left(\frac{m}{z}\right)_{lowest}$). This allows, for example, routine parallel detection of several of the most important biological ions with $^{12}C^-$ at 12.0000 $\frac{m}{z}$, $^{14}N^{12}C^-$ for measuring N at 26.0031 $\frac{m}{z}$, $^{31}P^-$ at 31.9738 $\frac{m}{z}$ and $^{32}S^-$ at 31.9721 $\frac{m}{z}$ as well as their minor isotopes, $^{13}C^-$ at 13.0034 $\frac{m}{z}$, $^{15}N^{12}C^-$ at 27.0001 $\frac{m}{z}$ and $^{34}S^-$ at 33.9679 $\frac{m}{z}$. However, due to the low mass of hydrogen, simultaneous measurement of $^1H^-$ at 1.0078 $\frac{m}{z}$ and $^2H^-$ at 2.0141 $\frac{m}{z}$ can only be combined with other ions up to a mass to charge ratio of ~22.2, which allows multi-isotope imaging for H and C in parallel, but not H and N in parallel. This restriction provides a serious impediment to the use of hydrogen-labelled isotopic tracers in combination with nitrogen (both an important isotopic tracer and identifying ion for organic material).

One approach to this problem is to use the instrument in magnetic field switching mode, which requires alternating magnetic field strengths for various ions in subsequent frames of the same analysis. However, this approach precludes simultaneous detection of all ions and is significantly more time consuming because of the need for sequential analyses and frequent cycling of the magnetic field. An alternative approach was employed by Lozano and colleagues (2013) to measure the $^{12}C^2H^-$ versus $^{12}C^1H^-$ ions with a NanoSIMS 50L in experiments with highly ^2H enriched sphingomeylin lipids [$^{2H}F \approx 40$ atom percent (at%)] as tracers, with corrections for isobaric interferences from $^{13}C^1H^-$ and $^{12}C^2H^-$. Although further improved by modifying the entrance slit (Slodzian *et al.*, 2014), the typical abundance sensitivity achievable on a NanoSIMS 50L is limited in resolving these interferences for environmental tracer experiments with relatively small enrichments close to natural abundance ^2H (Doughty *et al.*, 2014). Another potential method proposed by Slodzian and colleagues (2014) takes advantage of the deflection plates located in front of the electron multipliers to use electrostatic peak switching for quasi-simultaneous detection of $^{12}C_2{}^2H^-$ and $^{12}C^{14}N^-$ (both nominally at 26 m/z) without magnetic field switching. However, truly simultaneous detection is not possible and significant isobaric interferences include $^{13}C_2{}^-$, $^{12}C^{13}C^1H^-$ and $^{12}C_2{}^1H_2{}^-$.

In this study, we present an approach for the simultaneous analysis of three biologically relevant isotope systems (hydrogen, carbon and nitrogen) in microbial populations by NanoSIMS. We establish the necessary calibration for the use of ^2H_2O in single-cell stable isotope tracer work with native and embedded microorganisms (*Staphylococcus aureus* as a model Gram-positive and *Pseudomonas aeruginosa* as a model Gram-negative organism) at environmentally relevant levels of ^{13}C, ^{15}N and ^2H enrichment. We demonstrate the combined application of heavy water and ^{15}N ammonium isotope tracers in a study of microbial activity and population heterogeneity of *S. aureus* during growth in continuous culture with generation times ranging from hours to weeks.

Results and discussion

Simultaneous NanoSIMS analysis of H, C and N isotopes

The combination of heavy water labelling with other commonly used C and N-based isotope tracers for NanoSIMS analysis is technically challenging because of the typical limitations in dynamic mass range encountered in multi-collector SIMS instruments (~22:1). For this study, we extended the position of detector trolley #1 past its official maximum configuration in our CAMECA NanoSIMS 50L multi-collection assemblage, gaining an effective mass range of 28:1. This configuration precluded the need for any magnetic or electric field switching and allowed for truly simultaneous detection of the $^1H^-$, $^2H^-$, $^{12}C^-$, $^{13}C^-$, $^{14}N^{12}C^-$ and $^{15}N^{12}C^-$ ions with key isobaric interferences well resolved (mass resolution for $^{13}C^-$, $^{14}N^{12}C^-$ and $^{15}N^{12}C^-$ was 4560, 7530 and 8800, respectively). Because there are no isobaric interferences for $^1H^-$ and $^2H^-$ with this analytical set-up, small isotopic enrichments of ^2H can be detected and quantified.

Measurement of the ^1H and ^2H ions requires a strong primary beam current because of the low ionization efficiency of hydrogen. In balancing primary beam current, pre-sputtering and analysis time, additional complications arise from the destructive nature of the technique and the faster detection of nitrogen. Pre-sputtering is a process where the sample is bombarded with a higher primary beam current for a short amount of time prior to data collection in order to embed primary ions (Cs^+) in the sample matrix (Hoppe *et al.*, 2013). This greatly improves ionization efficiency, and consequently provides higher secondary ion counts during analysis, but also degrades the sample and changes ionization efficiency differentially depending on the ions. Figure 2 illustrates the change in ion counts per millisecond, both quantitatively (Fig. 2A)

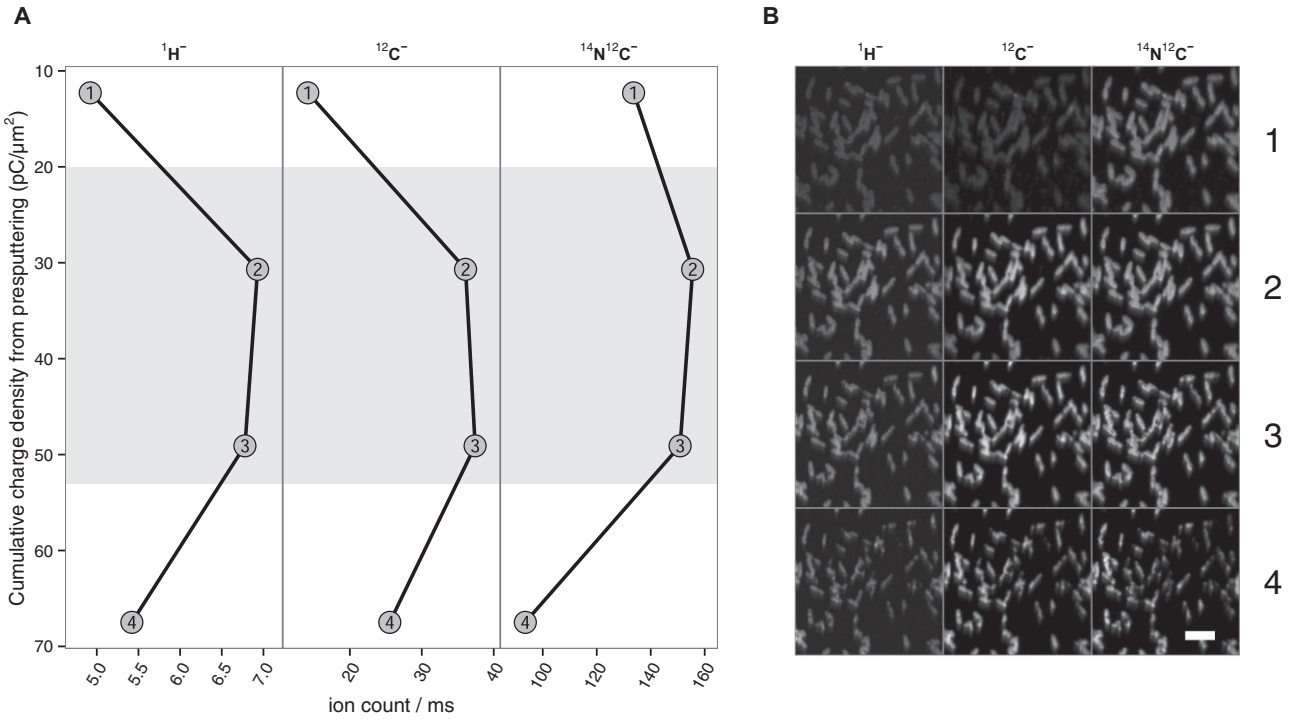

Fig. 2. Ionization efficiency and sample ablation in single-cell analysis.
A. Ion counts of the major H, C and N ions after various extents of primary ion beam exposure (quantified as cumulative charge density $I_{pre} \cdot t/A$ from pre-sputtering with primary Cs^+ beam current $I_{pre} \approx 23$ pA). The grey band indicates the analytical window targeted in this study.
B. 15 μm × 15 μm ion images recorded at the different points (1–4) indicated in A, showing a group of individual *P. aeruginosa* cells. For each ion, the maps are normalized to the highest signal intensity for ease of comparison between ions in the side-by-side visualization. Scale bar is 3 μm.

and visually (Fig. 2B), for the major isotopes' ions ($^{1}H^{-}$, $^{12}C^{-}$, $^{14}N^{12}C^{-}$) as a function of exposing the sample surface [here, a cluster of single whole cells of *P. aeruginosa* on conductive indium tin oxide (ITO)-coated glass] to the primary ion beam. The figure shows how Cs^+ beam sputtering increases ionization efficiency up to a maximum, at which point the sample is increasingly degraded, and ion counts drop as the organic material disappears. The major ion maps in Fig. 2 illustrate this visually and also highlight the faster detection of nitrogen. This effect requires adapting analytical conditions to optimally capture secondary ions prior to cellular degradation. The corresponding analytical window targeted in this study for all analyses of whole single cells is indicated by the grey band in Fig. 2A. Corresponding data on ionization efficiency and sample ablation during analysis of plastic embedded cells is provided in Appendix S3.

Single-cell calibration

To calibrate the simultaneously acquired measurements of hydrogen, carbon and nitrogen isotopic composition of single cells by NanoSIMS, we compared single-cell values of isotopically labelled homogenous cultures of *S. aureus* and *P. aeruginosa* to their independently measured bulk isotopic composition (see Table S9.1 in the Appendix for details). This calibration step is particularly important for hydrogen due to the high capacity for H exchange in organic material and the potential mass fractionation effects expected in the SIMS analysis for H isotopes. We elected to calibrate single-cell H isotope measurements against their respective bulk membrane fatty acid isotope composition because fatty acids represent a key non-exchangeable cellular H reservoir that can be measured rigorously at low ^{2}H enrichment. The calibration curve itself reflects all combined isotopic effects associated with sample preparation and analysis (loss, exchange, mass fractionation, combined H pools from all cellular components, etc.) and thus allows an empirical conversion of a single-cell NanoSIMS measurement into the representative enrichment of a cell component (the membrane) that is quantitatively interpretable. In light of this being the first application of multi-isotope imaging mass spectrometry with H, C and N simultaneously, it seemed prudent to also calibrate single-cell C and N isotope measurements against their respective bulk cell equivalents. Although natural abundance cells of *Escherichia coli* and spores of *Clostridia* (Davission *et al.*,

Table 1. Calibration parameters for single cell versus bulk isotope analysis.

Organism	Isotope	Calibration range [$^{x}F_{bulk}$ (*at*%)]	$^{x}F_{cells}$ versus $^{x}F_{bulk}$ slope	$^{x}F_{cells}$ versus $^{x}F_{bulk}$ intercept ^{x}F(*at*%)	R^2	Single-cell RSD[a]
P. aeruginosa	^{2}H	0.017–0.599	0.67 ± 0.05	0.0 ± 0.0	0.998	22%
S. aureus	^{2}H	0.013–0.689	0.59 ± 0.05	0.0 ± 0.0	0.997	19%
P. aeruginosa	^{13}C	1.1–10.7	0.73 ± 0.07	0.1 ± 0.2	0.997	1.6%
P. aeruginosa	^{15}N	0.36–10.25	0.94 ± 0.06	−0.0 ± 0.1	0.999	1.6%
S. aureus	^{15}N	0.36–4.50	0.91 ± 0.03	0.0 ± 0.0	1.000	5.7%

a. Relative standard deviation (RSD) of all single-cell measurements in the calibration (% of the measurement, not at%).
Calibration parameters were calculated from 1/x weighted linear regression of the average isotopic composition of all single cells ($^{x}F_{cells}$) for a given bacterial isotope standard (172 ROIs for *P. aeruginosa* and 222 ROIs for *S. aureus*) versus the measured bulk isotopic composition ($^{x}F_{bulk}$). All data are reported in fractional abundances ^{x}F (with x = ^{13}C, ^{15}N and ^{2}H, see *Experimental procedures* for details). Reported errors represent 95% confidence intervals from the regression.

2008; Orphan and House, 2009; Dekas and Orphan, 2011) as well as highly ^{15}N enriched (~50% ^{15}N) cells of *Pseudomonas fluorescens* (Herrmann *et al*., 2006) have been used as reference materials for isotopic analysis of whole single cells, to our knowledge, a multi-point calibration curve with enriched isotopic standards has only been reported previously in Time-of-flight-SIMS experiments with ^{15}N (Cliff *et al*., 2002) and does not exist for carbon or nitrogen analysis of free whole cells in NanoSIMS.

Calibration parameters were calculated from 1/× weighted linear regression of the average isotopic composition of all single cells for a given bacterial isotope standard versus the measured bulk isotopic composition, and are summarized in Table 1 for all isotopic standards tested in this study. In calculations of the average isotopic composition of all single cells for a given standard, individual cells were weighted inversely by the predicted Poisson error σ_F in their isotopic measurement (see Appendix S2 and Fitzsimons *et al*., 2000; Hayes, 2001 for details) to offset the influence of highly imprecise measurements from small regions of interest (ROIs) and low ion counts.

Figure 3 shows the calibration curves for single whole cell analyses of fixed *P. aeruginosa* (172 ROIs) and *S. aureus* (222 ROIs) respectively. As expected, the nitrogen isotope compositions of single cells for both

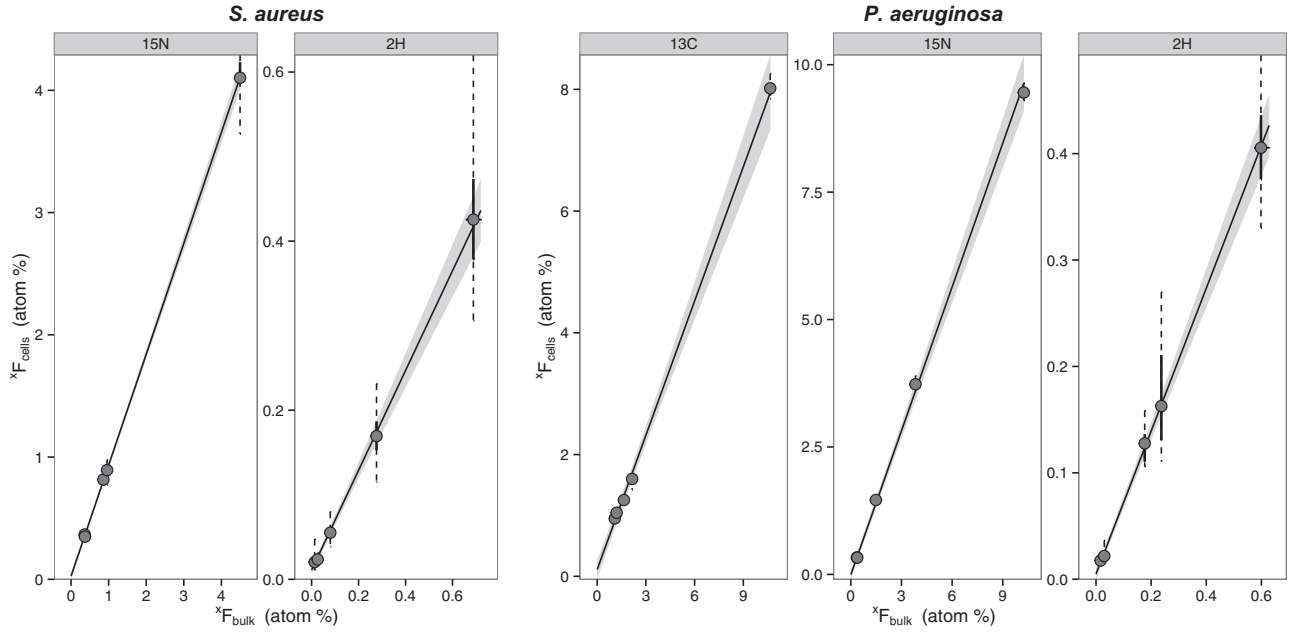

Fig. 3. Calibration curves for single cell versus bulk isotope analysis. Isotopic composition of bacterial isotope standards in single-cell analysis by NanoSIMS versus bulk analysis by EA-ir-MS (bulk ^{13}C and ^{15}N) and GC-pyrolysis-ir-MS (bulk fatty acid ^{2}H). All data are reported in fractional abundances ^{x}F (with x = ^{13}C, ^{15}N and ^{2}H). Data points represent the mean isotopic composition of all measured single cells. The solid vertical error bars for each data point represent the range that comprises 50% of the single-cell data. The dashed vertical whiskers represent the entire range of all single-cell measurements. Horizontal error bars represent the total range of measured bulk isotopic composition (smaller than symbol sizes in most cases). Linear regressions are shown with 95% confidence bands.

organisms mirror the bulk isotopic composition, with near perfect linear correlation and slope close to 1. However, it is important to note that both slopes fall slightly short of 1.0 (0.94 ± 0.06 and 0.91 ± 0.03), suggesting systematic dilution of the cellular isotopic signal from trace nitrogen on ITO-coated glass, systematic isotope fractionation in the analytical process (mass fractionation effects in SIMS analysis typically deplete isotope ratios by 1–10% in the heavier isotope, Fitzsimons *et al*., 2000) or potential variability of the cellular components due to preparation for SIMS analysis (fixation, dehydration and storage in ethanol). Background analysis of nitrogen ion counts on ITO-coated glass indicates that this component, while present, contributes only negligible amounts of nitrogen to the signal (data not shown). Since isotope ratios and fractional abundances of single cells are derived here directly from NanoSIMS ion count measurements without comparison to an authentic reference standard, fractionating effects during ionization and analysis likely contribute to the observed discrepancy. The relative standard deviation (RSD, in per cent of the measurement) of the single-cell measurements of each calibration curve provides an estimate of the measurement uncertainty from the combination of both analytical error as well as biological variation in the standards (Table 1). In the case of nitrogen, the RSD for the *S. aureus* standards (5.7%) suggests higher biological variability in single-cell nitrogen than for *P. aeruginosa* (RSD of 1.6%), which is consistent with the wider range of potential nitrogen sources available in the *S. aureus* medium because of the organism's auxotrophy for several amino acids (see *Experimental procedures*).

The carbon isotope composition of single *P. aeruginosa* cells (no ^{13}C standards were prepared for *S. aureus*) closely follows the bulk isotopic composition but also falls short, with a slope of 0.73 ± 0.07. This also suggests a combination of systematic dilution and isotopic fractionation during analysis. Background analysis also indicates a maximal contribution of organic carbon adhered to the ITO-coated glass of ~3%. However, in the case of carbon, fixed single cells are expected to be slightly offset isotopically from the unfixed bulk population due to the introduction of near natural abundance carbon in formaldehyde. Musat and colleagues (2014) recently reported this effect to account for a ~4% dilution of cellular carbon in experiments with *Pseudomonas putida*, which could explain part of the observed offset in the calibration. Even stronger isotope dilution effects have been observed in more elaborate pre-treatment procedures, such as catalysed reporter deposition fluorescence *in situ* hybridization (Woebken *et al*., 2014), and must be taken into consideration for experiments involving this approach.

Finally, the hydrogen isotope composition of single cells for both organisms show a robust linear dependence on the bulk membrane fatty acid isotopic composition. The slope is substantially lower than unity (0.67 ± 0.05 for *P. aeruginosa* and 0.59 ± 0.05 for *S. aureus*). This is consistent with the expected effects of hydrogen exchange. While the measured bulk isotopic composition is based on non-exchangeable hydrogen incorporated into membrane fatty acids, the ^{2}H content of individual cells measured by NanoSIMS is necessarily based on the integrated signal from all cellular hydrogen. Here, we employed a strict multi-step washing protocol for all cultures, with the goal of exchanging all readily exchangeable hydrogen with natural abundance H in the washing solutions. The calibration should allow for conversion of single-cell measurements to bulk fatty acid ^{2}H for cells treated identically. The calibration parameters inferred for *P. aeruginosa* and *S. aureus* suggest, however, that there can be a substantial degree of variability between individual organisms. The observed pattern indicates that *S. aureus* cells contain a higher proportion of hydrogen that exchanges during these washing steps (lower slope) than *P. aeruginosa* (higher slope), which is consistent with the Gram-positive (one lipid membrane instead of two), spherical (lower surface to volume ratio) *S. aureus* containing a lower proportion of lipid bound hydrogen than the Gram-negative (two lipid membranes), rod-shaped *P. aeruginosa*. In the absence of any isotope fractionation in the detection of hydrogen during NanoSIMS analysis, the observed slopes would indicate that about ~40% of the hydrogen was exchanged with water during the washing steps for *S. aureus*, and ~30% for *P. aeruginosa*. Lastly, single-cell isotopic measurements of hydrogen show substantial variability around the mean for both *S. aureus* (RSD of 19%) and *P. aeruginosa* (RSD of 22%), which likely reflects both the statistical uncertainty in the measurements for each single cell from low ion counts of ^{2}H, as well as random variation in the exact cellular components (highly exchangeable versus non-exchangeable parts of the cell) sampled by the ion beam during analysis. This aspect of hydrogen isotope measurements of single cells by SIMS is a fundamental constraint that limits the ability to resolve small isotopic differences between individual cells, and requires the analysis of many cells (tens to hundreds) within a microbial population if isotopically similar communities need to be distinguished.

This calibration provides the empirical parameters for inferring the bulk (whole membrane) hydrogen isotopic composition from the analysis of single whole cells of *S. aureus* and *P. aeruginosa*, with the statistical caveats outlined above. While this calibration is likely applicable to other Gram-negative and Gram-positive cells of

similar morphology that are prepared identically for NanoSIMS analysis, extrapolation to other microorganisms has to be interpreted with care. We applied this calibration to study the distribution of single-cell growth rates in continuous culture of *S. aureus* as described below.

We also measured all bacterial isotopic standards in plastic embedded thin section to provide a calibration for NanoSIMS measurements of sectioned samples. Multi-isotope imaging mass spectrometry in thin section vastly expands the range of applicability of this technique to large complex systems, such as highly structured microbial communities (e.g. biofilms and microbial mats; Fike *et al*., 2008; Woebken *et al*., 2012; Wilbanks *et al*., 2014) or communities associated with plants and animals (e.g. commensal and symbiotic relationships; Lechene *et al*., 2007; Berry *et al*., 2013). The structural support lent by the plastic matrix provides thin sections with a flat surface that enables high spatial resolution in imaging mass spectrometry due to the lack of strong topological features. It also retards sample destruction by the ion beam. However, plastic resins also contribute significant amounts of carbon and hydrogen that dilute the isotopic signal of enriched cells. It is thus imperative to calibrate and correct any isotopic measurements of single cells embedded in plastic and we present details on this calibration in Appendix S3, which should be useful for future NanoSIMS studies requiring embedding prior to analysis.

Single-cell growth diversity in continuous culture

Both environmental and laboratory populations exhibit significant metabolic variation at the single-cell level. This heterogeneity is a fundamental aspect of the ecological function and metabolic versatility of microbial communities, yet it is notoriously difficult to capture analytically at the population level. Here, we demonstrate the combined use of hydrogen and nitrogen isotope labelling with SIMS to study the activity, heterogeneity and substrate preferences of individual cells in microbial populations growing at different growth rates under controlled conditions in a chemostat. We focused on the common nocosomial pathogen *S. aureus* for these extended growth experiments to minimize the risk of population heterogeneity by physical differentiation through the formation of biofilms, which is of considerable concern with *P. aeruginosa*. *Staphylococcus aureus* was grown in continuous culture with three different dilution rates (corresponding to generation times of ~6 h, ~1 day and ~2 weeks), and spiked at steady state simultaneously with both a ^2H_2O isotope label ($^{2H}F_{water} = 0.248$ at%, 0.246 at% and 0.275 at%) as well as a $^{15}NH_4^+$ label ($^{15N}F_{NH_4^+} = 28.0$ at%, 24.9 at%, 25.0 at%) as described in the *Experimental procedures*. Samples were withdrawn at regular intervals within half of a generation time for each experimental set-up. The hydrogen and nitrogen isotopic composition of individual cells was measured by multi-isotope NanoSIMS and single-cell isotopic values were converted to their corresponding bulk population equivalents using the calibrations for *S. aureus* cells presented earlier (overview of single-cell data in Fig S9.1 in the Appendix). The growth activity rate $\mu_{act} = \mu + \omega_{fa}$ (representing the combined cellular replication rate μ and fatty acid turnover ω_{fa}) was calculated from the hydrogen isotope measurements for each cell using the equations outlined in Appendix S6.

Table 2 summarizes the results and Fig. 4A shows the aggregated data for single-cell growth activity rates μ_{act} measured from the three continuous culture experiments in comparison with the experimentally set dilution rates for each culture (representing the expected average replication rate μ). Overall population growth is slightly underestimated by single-cell data in the fastest growing culture (6.38 h), and overestimated at the intermediate (1.24

Table 2. Summary of single-cell growth rates of *S. aureus* in continuous culture measured by isotope labelling with ^2H_2O.

Dilution rate (h^{-1})	Generation time	Analysed single cell	Single-cell ^{2H}F RSD[a]	Median single-cell growth rate $\bar{\mu}_{act}$ (h^{-1})	Single-cell growth rate range (50% of data)	Levene's test *P* value[b]	Single-cell ^{15N}F RSD[a]
		Standards	19%	0.102	$0.65 \cdot \bar{\mu}$ to $1.40 \cdot \bar{\mu}$	$\rangle$ 0.008**	5.7%
0.109	6.38 h	293	27%	0.076	$0.50 \cdot \bar{\mu}$ to $1.70 \cdot \bar{\mu}$		40%
0.023	1.24 days	296	31%	0.053	$0.51 \cdot \bar{\mu}$ to $1.80 \cdot \bar{\mu}$	$\rangle$ 0.02*	47%
0.002	13.34 days	188	51%	0.005	$0.31 \cdot \bar{\mu}$ to $3.50 \cdot \bar{\mu}$	$\rangle < 0.0001$****	93%

a. Relative standard deviation (RSD) of the single-cell isotopic measurements (for H and N respectively).
b. *P* value of the Brown-Forsythe (median-based) Levene-type test statistic for equality of variances between the paired ⟨⟩ growth rate distributions of each consecutive rows, lower *P* value indicates higher probability that the variances are *different*.
Chemostat parameters are derived from experimental set-up. Statistical parameters for each experiment are derived from all individual cells. First line (Standards) is a simulated data set produced from all single-cell measurements of the bacterial standards (Table 1) scaled to the mean of the first data set (generation time of 6.38 h) for statistical comparison and to evaluate propagation of the standards' measurement error (RSD) through the entire growth rate evaluation calculations (see Appendix S6 for details).

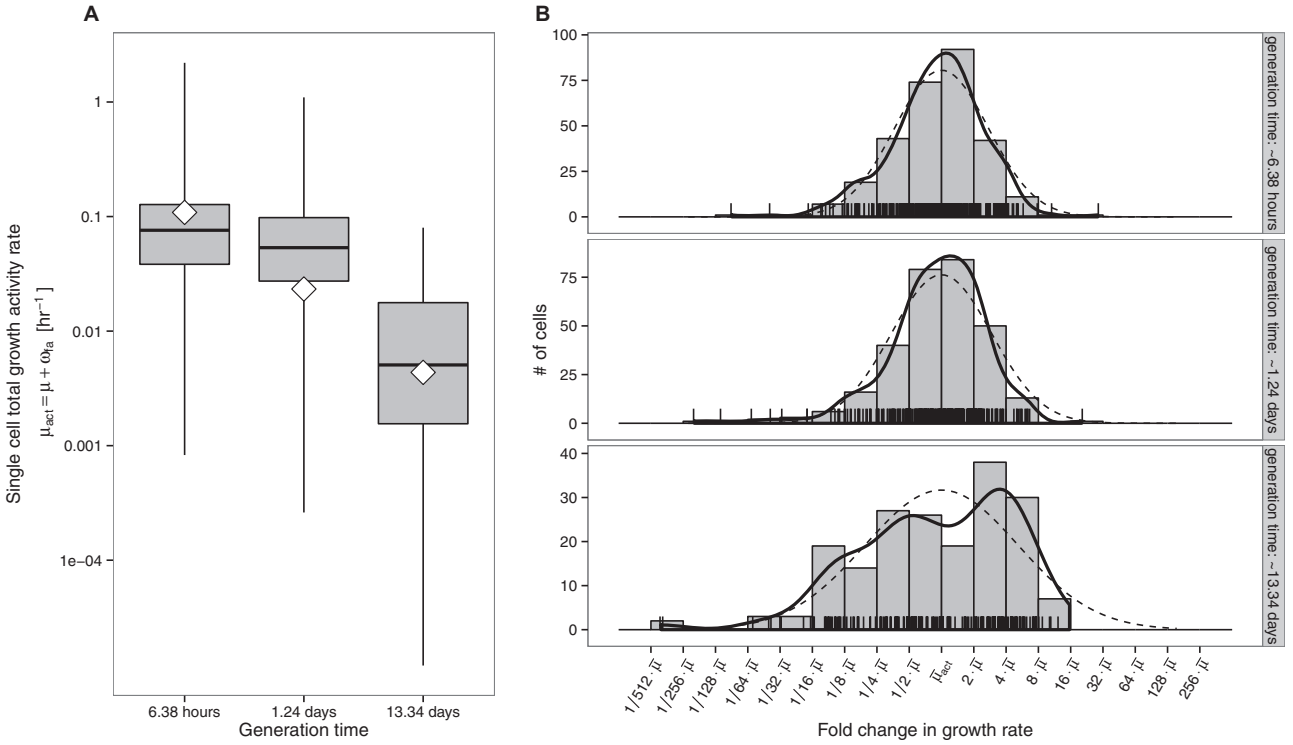

Fig. 4. Single-cell growth rates of *S. aureus* in continuous culture measured by isotope labelling with ^2H_2O.
A. Box plots of single-cell growth activity rates ($\mu_{act} = \mu + \omega_{fa}$, representing the combined cellular replication rate μ and fatty acid turnover ω_{fa}). Grey bands for each continuous culture experiment represent the range comprising 50% of the single-cell data with the black lines indicating the median $\bar{\mu}_{act}$. Whiskers represent the entire range of single-cell data. White diamonds represent the experimentally set dilution rate for each culture (equivalent to average population replication rate μ).
B. Histograms of single-cell growth rates normalized to the median $\bar{\mu}_{act}$ for each experiment. All data are plotted on a logarithmic scale. The solid black line shows an estimate of the probability density function that represents the data. The dashed line shows the best fit to a log-normal distribution (i.e. a normal distribution of the log-transformed data). Short vertical black lines show all individual data points.

days) and slowest (13.34 days) generation times. Overestimates at slower growth rates are potentially a consequence of the turnover component (ω_{fa}). Turnover represents the rate of molecular replacement, that is, fatty acid degradation and production in excess of the biosynthetic rate required purely for cellular replication (μ). Hydrogen from the water isotope tracer is incorporated in both processes and only their combined effect, the overall biosynthetic/growth activity rate (μ_{act}), can be captured at the single-cell level. Bacteria are known to modulate the fatty acid composition of their membranes in response to physical and chemical changes in their environment (Zhang and Rock, 2008), but little is known about fatty acid turnover in bacteria growing at steady state in a chemically stable environment.

The most striking observation, however, is the diversity in cellular activity rates revealed by our data. For comparison, Table 2 includes a simulated dataset produced from all single-cell measurements of the bacterial standards (Table 1) scaled to the mean of the fastest continuous culture condition (generation time of 6.38 h). The RSDs of the single-cell hydrogen isotope measurements themselves suggest an increase in heterogeneity from the standards, which reflect exponential growth in batch culture, to the chemostat cultures. Typically, well mixed steady-state chemostat cultures are considered to be among the most homogenous microbial populations in any experimental system due to the constant medium composition and lack of chemical gradients. While the possibility of spatial differentiation in the chemostat vessels cannot be ruled out, *S. aureus* does not typically form biofilms in this medium, and careful inspection of the vessels after termination of each experiment revealed no cellular attachment. This implies either phenotypic or genotypic differentiation. The observed diversity would not be possible to detect in bulk physiological or isotopic measurements and is revealed here only by inspection at the single-cell level. Single-cell activity rates appear to be log-normally, rather than normally, distributed (illustrated in Fig. S8.1 in the Appendix). Figure 4B shows the histograms and estimated probability density functions for the log-transformed data together with the best fit approximation to log-normal distributions. Differences in the heterogeneity between the simulated standards

dataset and the chemostat cultures is evaluated statistically by comparing the variances of the growth rate distributions, as listed in Table 2. The observed pattern suggests that the fastest continuous culture condition (generation time of 6.38 h) is significantly more heterogeneous than the standards (P value < 0.01) with a less significant increase from the fastest to the next slower (1.24 days) continuous culture (P value < 0.05). The most significant increase in heterogeneity is seen in the slowest growth condition (P value < 0.0001). It is noteworthy that the distribution of single-cell growth rates at the slowest growth condition hints at a possible bimodal activity pattern with two distinct subpopulations. No clear pattern as to a dependence of growth activity on cell size could be distinguished and it remains an open question what physiological differences precipitate the diversity of activity rates observed for *S. aureus*, and what mechanisms give rise to the diversification. Slight differences in metabolic strategy, for example, could be a potential source of single-cell diversity, and could arise from either genetic diversification, or through stochastic gene expression and other purely phenotypic diversification mechanisms. Previous work on mixed culture chemostats has highlighted microbial assemblages that are functionally stable yet can undergo dramatic phylogenetic variation within the community (Fernández *et al*., 1999), but genotypic and phenotypic diversification do not require mixed cultures, both have been observed even for single species in homogenous conditions. Maharjan and colleagues (2007), for example, measured metabolic diversification of initially clonal, single-species populations of *E. coli* grown in glucose limited chemostats after 90 generations, and showed evidence for differentially evolving subpopulations adopting different metabolic strategies for substrate use. Nikolic and colleagues (2013), on the other hand, studied gene expression of clonal populations of *E. coli* in similar glucose-limited chemostats after ~7 generations, and showed evidence for heterogenous expression of metabolic genes. While both mechanisms do likely occur in parallel, the latter (phenotypic diversification) is more likely to play a dominant role at the generational time scales of this study (four to six generations). Lastly, it is also noteworthy that observations in long-term experiments of stationary phase cultures suggest that at any point in time, the population consists of genetically distinct subpopulations that are dynamically increasing and declining over time (Finkel, 2006). While this growth advantage in stationary phase (GASP) phenotype of different subpopulations is mostly reported in the context of batch cultures where chemical conditions are not constant, it is possible that a slow growing chemostat provides an environment that similarly supports increased heterogeneity within the culture.

Single-cell ammonium utilization

In the continuous culture experiments in this study, *S. aureus* has access to both inorganic and organic nitrogen sources in the form of ammonium and various amino acids (details in *Experimental procedures*). A single isotopic tracer based on nitrogen (here, $^{15}NH_4^+$) thus integrates a mixed signal that is affected both by growth, as well as the cells' nitrogen preference. The RSDs of the nitrogen measurements reported at the end of Table 2 already suggest a stronger diversification in nitrogen (from 5.7% RSD in the standards to 93% in the slowest growing culture) compared with hydrogen (from 19% to 51%), pointing to pronounced differences in single-cell nitrogen preferences. Constraining growth activity independently by using ^2H_2O as an additional isotope tracer allowed us to deconvolve the ^{15}N signal and infer ammonium utilization on a single-cell basis. For each cell, the fraction of nitrogen assimilated from ammonium ($x_{NH_4^+}$) was estimated from the ^{15}N isotope labelling strength and the hydrogen-derived growth rate, as detailed in Appendix S6. It is important to note that the hydrogen-derived growth activity rates (μ_{act}) include a component of fatty acid turnover (ω_{fa}) that is unlikely to be representative of cellular nitrogen turnover (ω_N). To account for this difference, we estimated cellular nitrogen turnover from known rates of protein turnover, considering the vast majority of cellular nitrogen is bound in proteins (Bertilsson *et al*., 2003), and assuming ammonium incorporation to occur during turnover. Protein turnover in bacteria has been studied most extensively in experiments with *Escherichia coli*, which suggest turnover rates can range from less than 0.25% h^{-1} for rapidly growing batch cultures to 4–5% h^{-1} for non-growing cells (Podolsky, 1953; Koch and Levy, 1955; Ernest Borek, 1958; Mandelstam, 1960; Mandelstam and Halvorson, 1960; Marr *et al*., 1963), with similar ranges observed in studies with *Bacillus cereus* (Urbá, 1959) and yeast (Pratt *et al*., 2002). Pine (1970; 1972) studied protein turnover specifically in continuous culture at varying generation times and found turnover rates to be fairly constant between 2.5% h^{-1} (glucose based growth) and 3% h^{-1} (acetate based growth), independent of growth rate. For this study, we thus used $\omega_N = 2.75\%\ h^{-1}$ as an estimate for turnover during steady-state growth with a mixture of carbon sources.

Figure 5A shows the aggregated data for single-cell ammonium assimilation, indicating the range and median value of nitrogen assimilation from ammonium (versus amino acids) in each continuous culture experiment. The data indicate that the majority of all cells derive less than ~50% of their nitrogen from ammonium. Such a significant contribution of amino acid-derived nitrogen ($1 - x_{NH_4^+}$) is consistent with known nutritional requirements of *S. aureus* (Mah *et al*., 1967; Lincoln *et al*., 1995). The

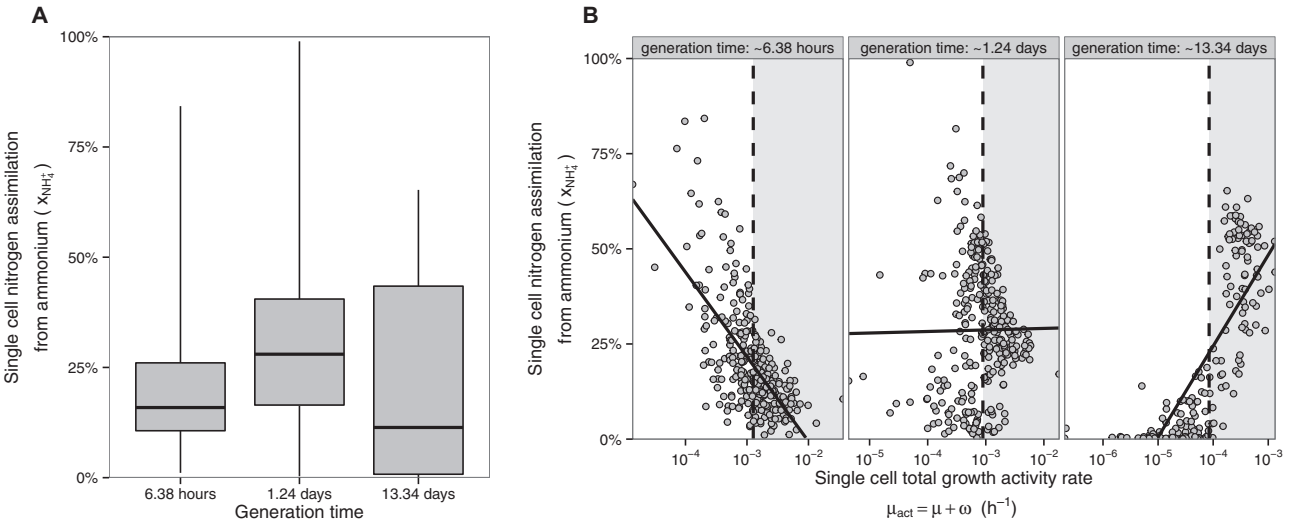

Fig. 5. Single-cell ammonium utilization of *S. aureus* in continuous culture measured by isotope labelling with ^2H_2O and $^{15}N\ NH_4^+$.
A. Box plots of single-cell nitrogen assimilation from ammonium ($x_{NH_4^+}$). Grey bands for each continuous culture experiment represent the range comprising 50% of the single-cell data with the black lines indicating the median. Whiskers represent the entire range of single-cell data.
B. Correlation plot between cell-specific nitrogen assimilation from ammonium ($x_{NH_4^+}$) and growth activity rate (μ_{act}), showing how ammonium assimilation changes with growth above/below the median within each population. Dashed vertical lines indicate the median growth activity rate with grey background above the median and white background below the median.

precise values of the average nitrogen assimilation depend on the exact protein turnover rate, which is estimated from literature values. Future work that further constrains protein turnover will enable more quantitative assessment of the exact partitioning between N assimilation from inorganic and organic sources both in laboratory and environmental studies.

The most striking observation, however, is the correlation between cell-specific use of ammonium and growth activity illustrated in Fig. 5B. Ammonium utilization in the fastest growing culture is negatively correlated (Spearman correlation = –0.63, P value < 10^{-30}), whereas the intermediate growth condition does not show a statistically significant correlation, and the slowest growing culture is instead positively correlated (Spearman correlation = 0.80, P value < 10^{-30}). This indicates that cells within a population of *S. aureus* that is growing relatively fast on average (generation time of 6.38 h) assimilate more nitrogen from amino acids when they are growing above the median rate (grey area in panel 1, Fig. 5B), whereas cells within a population that is growing relatively slow on average (generation time of 13.34 days) assimilate more nitrogen from ammonium when they are growing faster than their peers (grey area in Fig. 5B, panel 3). These data do not reveal the nature of any potential causal relationship underlying this correlation, but they potentially suggest that utilizing amino acids over ammonium is the optimal strategy for *S. aureus* only in relatively fast growing cultures (generation time of ~6 h, Fig. 5B, panel 1) and becomes less advantageous (generation time of ~1.2 days, Fig. 5B, panel 2), or even disadvantageous at slower growth and nutrient fluxes (generation time of ~13.3 days, Fig. 5B, panel 3). This overall pattern of a transition from positive to negative correlation of ammonium uptake with cellular growth activity between the slower growth and fast growth conditions holds up independent of precise protein turnover rates, although we are only just beginning to uncover these single-cell metabolic differences.

Important constraints on the quantitative use of ^2H_2O labels

For practical application, it is important to note that labelling concentrations above the maximum of 20% ^2H_2O pictured in Fig. 1 are not recommended, because at higher concentrations the heavy isotope starts to significantly affect the solvent properties of water and substitutes for ^1H in functional groups, disturbing biological macromolecules. Most organisms including mammals and insects are usually unaffected by doses of up to ~10%. Although microorganisms can be unaffected by concentrations as high as 20–30% (Kushner *et al*., 1999), it is important to assess potential inhibitory effects for all targeted microorganisms in an environmental sample when using elevated concentrations of ^2H_2O above ~10%, because the (partial) inhibition of certain organisms could severely bias activity measurements. We tested the susceptibility of *S. aureus* to varying doses of ^2H_2O in the medium used in this study, and observed the toxicity threshold to fall between 15%

and 20% ^2H_2O (see Appendix S5 for details). In the absence of representative laboratory cultures, toxicity thresholds could be assessed directly in environmental samples by monitoring metabolic output (for example, the rate of sulfate reduction or oxygen respiration) in response to increasing ^2H_2O spikes. Generally, ^2H_2O spikes are best used at low doses. In this study, we thus focused specifically on testing ^2H_2O labelling methods at low ^2H_2O concentrations (< 0.3 at%) with the goal of environmental application in mind.

For quantitative assessments of ^2H enrichment, it is also important to consider that the anabolic incorporation of hydrogen from water can vary significantly in response to physiological differences (especially autotrophic versus heterotrophic growth strategies) and substrate preferences (Sessions and Hayes, 2005; Valentine, 2009; Zhang *et al*., 2009) and should also be assessed carefully for all targeted microorganisms in an environmental sample. For this study, we determined the key physiological parameters for water hydrogen assimilation into fatty acids specifically for *S. aureus* following the approach of Zhang and colleagues (2009), and report the results in detail in Appendix S6.

Conclusion

As we have demonstrated, single-cell multi-isotope labelling with heavy water in combination with ^{13}C and ^{15}N stable isotope tracers can complement traditional spatiometabolic stable isotope studies by providing the context of baseline microbial activity. The use of heavy water as a non-toxic (at concentrations < 10%), fast-diffusing, chemically conservative tracer, combined with the ability to measure relatively small ^2H enrichments at the single-cell level ($^{2H}F \approx 0.1$ at%), allows microbial activity measurement in a wide range of environmental systems. These range from natural habitats where microorganisms are growing very slowly to *in-vivo* studies where microbial activity is set in response to host-derived growth factors, toxins or other effectors.

Our data reveal heterogeneity in cellular activity at the single-cell level even in populations grown under tightly controlled laboratory conditions in continuous culture. Moreover, at this level of resolution, differences in nitrogen assimilation patterns are evident within populations growing at different rates. Future studies will have to determine whether this phenomenon simply reflects random variation between *S. aureus* populations, or perhaps is indicative of a much broader physiological adaptation that is causally linked to turnover rates. Regardless, it is clear that this approach could provide insight into important physiological processes that elude batch analysis. Going forward, the combination of heavy water labelling with specific ^{13}C and ^{15}N-labelled substrates, in particular, will enable studies to measure the assimilation of a target substrate at the single-cell level even in organic-rich environments (for example, soils, biofilms, microbial mats and tissues) while also providing, at the same time, a clear context for activity of all members of the community independent of their use of the target substrate. Similarly, substrate assimilation studies in oligotrophic environmental systems can be understood in the context of overall community activity and can shed light on the direct and indirect impacts of added nutrients.

Experimental procedures

Bacterial isotope standards

Bacterial hydrogen, carbon and nitrogen isotopic standards for single-cell analysis were created by growing a Gram-positive organism, *S. aureus* (MN8, Kreiswirth *et al*., 1983), and a Gram-negative organism, *P. aeruginosa* (PA14, Rahme *et al*., 1995), with nutrients of different isotopic composition. A phosphate-buffered minimal medium at pH 7.2 containing 2.5 g l^{-1} NaCl, 13.5 g l^{-1} K_2HPO_4, 4.7 g l^{-1} KH_2PO_4, 1 g l^{-1} K_2SO_4 and 0.1 g l^{-1} $MgSO_4{\cdot}7H_2O$ served as the basis for all experiments. *Pseudomonas aeruginosa* was grown in this medium with different amounts of ^2H_2O (up to 1%, prepared from a 70% stock solution, Cambridge Isotope Laboratories, #DLM-2259-70-1L), 10 mM ammonium chloride (spiked up to 10% ^{15}N with 98% enriched $^{15}NH_4Cl$, Sigma-Aldrich, #299251) and 10 mM sodium succinate (spiked up to 10% with 99% enriched succinic-1,2-$^{13}C_2$ acid, Sigma-Aldrich, #491977). *Staphylococcus aureus* was grown in this medium with different amounts of D_2O, 10 mM ammonium chloride (both spiked identically to *P. aeruginosa* cultures) and 10 mM glycerol (^{13}C labelling experiments were not the focus of the study and isotopically labelled glycerol was unavailable for the standards at the time). *Staphylococcus aureus* further exhibits auxotrophy for several amino acids and vitamins (Mah *et al*., 1967; Lincoln *et al*., 1995; Aldeen and Hiramatsu, 2004) and the medium was amended with 11.5 mg l^{-1} proline, 10 ml l^{-1} 50x MEM Amino Acid solution (Sigma-Aldrich, #M5550, final amino acid concentrations: 63.2 mg l^{-1} arginine, 15.6 mg l^{-1} cysteine, 21 mg l^{-1} histidine, 26.35 mg l^{-1} isoleucine, 26.2 mg l^{-1} leucine, 36.3 mg l^{-1} lysine, 7.6 mg l^{-1} methionine, 16.5 mg l^{-1} phenylalanine, 23.8 mg l^{-1} threonine, 5.1 mg l^{-1} tryptophan, 18.0 mg l^{-1} tyrosine, 23.4 mg l^{-1} valine) and 100 μg l^{-1} thiamine (B1), 100 μg l^{-1} nicotinic acid (B3) and 10 μg l^{-1} biotin (B7) for all experiments with this organism.

All cells were grown in 50 ml batch cultures aerobically at 37°C, and were inoculated from fresh (exponential) cultures grown on the same medium. Cultures were harvested in mid-exponential phase to ensure as homogenous a population as possible for consistent isotopic composition. Cells were harvested by centrifugation at 4000 r.p.m. for 10 min at 4°C, and washed five times by resuspension in 1× phosphate-buffered saline (PBS) solution to remove all residual nutrients. Before the last washing step, samples were split into separate aliquots for bulk isotopic analysis and single-cell analysis. Aliquots for bulk analysis were pelleted,

frozen and stored at −80°C until further processing. Aliquots for single-cell analysis were fixed in 1% freshly prepared formaldehyde in PBS (Paraformaldehyde, Electron Microscopy Sciences, #15713) for 2 h at room temperature, washed once more in 1× PBS and dehydrated in 50% ethanol.

Continuous culture

Carbon-limited continuous culture experiments at different growth rates were carried out with *S. aureus* growing aerobically at 37°C in a Sartorius Biostat QPlus autoclavable chemostat system in the same medium used for the *S. aureus* isotope standards (without any isotope enrichment), and amended with 500 µl l^{-1} Antifoam 204 (Sigma Aldrich, #A6426). Chemostat vessels with ~550 ml working volume were inoculated from a single colony pre-grown in the same medium and continuous supply of medium was started upon reaching early stationary phase. Overflow from the vessels was continuously removed to maintain a fixed volume, and for each experiment, the exact dilution rate was determined gravimetrically from the total vessel content and medium flow rate. Redox potential, pH and dissolved oxygen were monitored continuously and optical density was measured in aliquots withdrawn aseptically from vessel overflow. Purity of the culture was checked periodically by light and once by epifluorescence microscopy using fluorescent *in situ* hybridization (Amann *et al*., 1990) with an *S. aureus*-specific 16S ribosomal RNA probe (5′ to 3′: GAAGCAAGCTTCTCGTCCG, Kempf *et al*., 2000). After the monitored physiological parameters reached steady state (usually within four to six generations), chemostat vessels were spiked with 2 ml 70% ^2H_2O and 150 mg $^{15}NH_4Cl$ isotope tracers, and samples for single-cell analysis were withdrawn directly from the vessel at regular intervals depending on the dilution rate. Dilution of the tracers from the continuous supply of fresh medium during incubation (to maintain steady-state growth conditions) was accounted for during data evaluation (see Appendix S6 for details). Samples were washed and fixed the same way as the bacterial isotope standards for single-cell analysis. Dehydrated cells were stored in 100% ethanol at 4°C and returned to 50% ethanol prior to analysis. The effective water isotopic composition of the medium in the chemostat vessels after the spike was monitored using a Los Gatos Research DLT-100 liquid water isotope analyser; the ammonium concentration was monitored using a Dionex DX-500 ion chromatography system with a 5·250 mm IonPac CS16 cation-exchange column and isocratic elution with 38% methanesulfonic acid at a flow rate of 2 ml min^{-1}.

Bulk analysis

All bulk analyses were carried out on homogenized dry biomass from lyophilized cell pellets. For nitrogen and carbon isotope analysis, 300 to 800 µg of cell powder were weighed out into tin capsules in duplicate, and the bulk carbon and nitrogen isotopic composition was determined by EA-ir-MS at the UC Davis Stable Isotope Facility (Davis, CA, USA).

For hydrogen isotope analysis, the average membrane fatty acid hydrogen isotopic composition was used as a measure of bulk ^2H incorporation because, unlike labile N–H or O–H bonds (Katz, 1960; Thomas, 1971), C–H bonds do not exchange hydrogen spontaneously (Sessions *et al*., 2004). Lyophilized cell pellets were weighed out into ~1 mg aliquots of dry cell mass, transesterified in the presence of acetyl chloride in anhydrous methanol (1:20 v/v) at 100°C for 10 min (Lepage and Roy, 1986; Rodríguez-Ruiz *et al*., 1998), extracted into hexane and concentrated under a stream of N_2 at room temperature. Fatty acid methyl esters were identified by gas chromatography/mass spectrometry on a Thermo-Scientific Trace DSQ, and analysed in triplicate for their isotopic composition by GC/pyrolysis/isotope-ratio mass spectrometry on a Thermo-Scientific Delta Plus XP. All data were corrected for the addition of methyl hydrogen during derivatization. Reported bulk hydrogen isotope compositions represent the mass balance weighted average isotopic composition of all major membrane fatty acids.

Single-cell analysis

One microlitre aliquots of fixed whole cells suspended in 50% ethanol (both isotopic standards and continuous culture samples) were spotted onto custom-cut, conductive ITO-coated glass (TEC15, Pilkington Building Products, Greensboro, NC, USA) and air-dried at room temperature. ITOs were mapped microscopically with a 40× air objective for later orientation and sample identification during SIMS.

All samples were analysed with a CAMECA NanoSIMS 50L (CAMECA, Gennevilliers, France) housed in the Division of Geological and Planetary Sciences at the California Institute of Technology. Whole cells on ITO were analysed using a ~3.6 pA primary Cs^+ beam current with a nominal spot size of ~300 nm and were pre-sputtered with a ~23 pA primary Cs^+ beam current (I_{pre}) for 3–6 min (t), depending on the size of the pre-sputtering area (A), to a cumulative charge density of ~20 pC μm^{-2} ($I_{pre} \cdot t/A$). Seven masses were collected in parallel ($^1H^-$, $^2H^-$, $^{12}C^-$, $^{13}C^-$, $^{14}N^{12}C^-$, $^{15}N^{12}C^-$, $^{28}Si^-$) using electron multipliers. Individual samples were located using the NanoSIMS CCD camera, and random analytical spots were chosen within a sample area. For all analyses, the beam was rastered over a square region of 10 µm by 10 µm for 15 min per analytical plane/frame. At least two frames were collected per analysis, and all ion images were recorded at 256 × 256 pixel resolution with a dwell time of 14 ms $pixel^{-1}$. Pre-sputtering was typically carried out on a larger region of at least 15 µm by 15 µm to make sure that the analytical frame was fully within the pre-sputtered area. Analytical parameters including primary beam focus, secondary beam centering and mass resolution for all ions were verified every ~30 min.

Quantification

Bulk carbon, nitrogen and hydrogen isotope measurements were recorded in the conventional δ-notation $\left(\delta^x = \frac{{}^xR_{sample}}{{}^xR_{ref}} - 1, \text{with x} = {}^{13}C, {}^{15}N, {}^{2}H\right)$ relative to the reference materials VPDB $\left({}^{13C}R_{VPDB} = \frac{{}^{13}C}{{}^{12}C} = 0.0112372\right)$, air $\left({}^{15N}R_{Air} = \frac{{}^{15}N}{{}^{14}N} = 0.003676\right)$ and VSMOW $\left({}^{2H}R_{VSMOW} = \frac{{}^{2}H}{{}^{1}H} = 0.00015576\right)$ respectively (de Laeter *et al*., 2003). To

allow consistent reporting and exact mass balance calculations (see Appendix S1 for details), all measurements were converted to fractional abundances $^{x}F\left(^{13C}F = \frac{^{13}C}{^{12}C + ^{13}C}, ^{15N}F = \frac{^{15}N}{^{14}N + ^{15}N}, ^{2H}F = \frac{^{2}H}{^{1}H + ^{2}H}\right)$ using the relation $^{x}F_{sample} = \frac{^{x}R_{sample}}{1 + ^{x}R_{sample}} = \frac{\delta^{x} + 1}{1/^{x}R_{ref} + \delta^{x} + 1}$. Fractional abundances of single-cell analyses were calculated directly from raw ion counts and calibrated against bulk measurements (see *Single cell calibration* for details). In this study, the fractional abundance values of most isotopically enriched standards and samples fall into the percent (10^{-2}) range, and are thus reported in atom percent (at%).

Raw data from all acquired ion images were processed using the open-source MATLAB plugin Look@NanoSIMS (Polerecky *et al.*, 2012). Ion images from multiple frames were corrected for dead time and quasi-simultaneous arrival (QSA) effect, aligned, and discrete ROIs were hand-drawn using the $^{14}N^{12}C^{-}$ ion images to identify the cellular outline of individual cells. All ROIs in this study represent individual single cells.

With the primary beam currents and analytical parameters employed in this study, single cells of *S. aureus* and *P. aeruginosa* typically supported the collection of up to three sequential frames before the primary ion beam ablated the cells. Two frames were collected routinely, and individual ROIs were screened for consistency between the isotopic values of two subsequent frames to control for higher quality data not distorted by sample destruction. ROIs with isotopic value F_i in any frame deviating by more than twice the shot noise $2{\cdot}\sigma_F$ (see Appendix S2 for details) and more than 1% from the frames' accumulated average F were discarded.

Single-cell total activity growth rates μ_{act} of *S. aureus* were calculated from the single-cell hydrogen isotope measurements (converted to bulk equivalents using the calibrations discussed in the text), sampling times, dilution rates and isotopic composition of the medium. μ_{act} represents the combined total biosynthetic activity from cellular replication rates μ and maintenance turnover ω. Ammonium assimilation $x_{NH_4^+}$ was estimated from single-cell nitrogen isotope measurements using hydrogen-based growth rate estimates. All relevant formulae are discussed in detail in Appendix S6. For each experimental condition, derived single-cell metrics (μ_{act} and $x_{NH_4^+}$) from all time points were combined for statistical analysis.

Acknowledgements

We thank Nathan Dalleska and the Caltech Environmental Analysis Center for instrumentation that benefited this project, Grayson Chadwick and Kat Dawson for helpful discussions, and members of the Newman and Orphan labs, as well as John Cliff and two anonymous reviewers for constructive criticism that improved the manuscript. This work was supported by grants from the Howard Hughes Medical Institute (HHMI) and the National Institutes of Health (Grant No. 5R01HL117328-03, to D.K.N.), and from the Gordon and Betty Moore Foundation (Grant No. GBMF3780 to V.J.O.). D.K.N. is an HHMI investigator. S.H.K. is an HHMI international student research fellow.

References

Aldeen, D.A., and Hiramatsu, K. (2004) *Staphylococcus Aureus. Molecular and Clinical Aspects*. Cambridge, UK: Woodhead Publishing.

Amann, R.I., Krumholz, L., and Stahl, D.A. (1990) Fluorescent-oligonucleotide probing of whole cells for determinative, phylogenetic, and environmental studies in microbiology. *J Bacteriol* **172:** 762–770.

Berry, D., Stecher, B., Schintlmeister, A., Reichert, J., Brugiroux, S., Wild, B., *et al.* (2013) Host-compound foraging by intestinal microbiota revealed by single-cell stable isotope probing. *Proc Natl Acad Sci USA* **110:** 4720–4725.

Bertilsson, S., Berglund, O., Karl, D.M., and Chisholm, S.W. (2003) Elemental composition of marine Prochlorococcus and Synechococcus: implications for the ecological stoichiometry of the sea. *Limnol Oceanogr* **48:** 1721–1731.

Cliff, J.B., Gaspar, D.J., Bottomley, P.J., and Myrold, D.D. (2002) Exploration of inorganic C and N assimilation by soil microbes with time-of-flight secondary ion mass spectrometry. *Appl Environ Microbiol* **68:** 4067–4073.

Davission, M.L., Weber, P.K., Pett-Ridge, J., and Singer, S. (2008) *Development of Standards for NanoSIMS Analyses of Biological Materials*. Livermore, CA: Laurence Livermore National Laboratory.

Dekas, A.E., and Orphan, V.J. (2011) Identification of diazotrophic microorganisms in marine sediment via fluorescence in situ hybridization coupled to nanoscale secondary ion mass spectrometry (FISH-NanoSIMS). *Methods Enzymol* **486:** 281–305.

Dekas, A.E., Poretsky, R.S., and Orphan, V.J. (2009) Deep-sea archaea fix and share nitrogen in methane-consuming microbial consortia. *Science* **326:** 422–426.

Doughty, D.M., Dieterle, M., Sessions, A., Fischer, W.W., and Newman, D.K. (2014) Probing the subcellular localization of hopanoid lipids in bacteria using nanoSIMS. *PLoS ONE* **9:** e84455.

Ernest Borek, L.P.D.R. (1958) Protein turnover in microorganisms. *Proc Natl Acad Sci USA* **44:** 369–374.

Fernández, A., Huang, S., Seston, S., Xing, J., Hickey, R., Criddle, C., and Tiedje, J. (1999) How stable is stable? Function versus community composition. *Appl Environ Microbiol* **65:** 3697–3704.

Fike, D.A., Gammon, C.L., Ziebis, W., and Orphan, V.J. (2008) Micron-scale mapping of sulfur cycling across the oxycline of a cyanobacterial mat: a paired nanoSIMS and CARD-FISH approach. *ISME J* **2:** 749–759.

Finkel, S.E. (2006) Long-term survival during stationary phase: evolution and the GASP phenotype. *Nat Rev Microbiol* **4:** 113–120.

Fitzsimons, I., Harte, B., and Clark, R.M. (2000) SIMS stable isotope measurement: counting statistics and analytical precision. *Mineral Mag* **64:** 59–83.

Foster, R.A., Kuypers, M.M.M., Vagner, T., Paerl, R.W., Musat, N., and Zehr, J.P. (2011) Nitrogen fixation and transfer in open ocean diatom–cyanobacterial symbioses. *ISME J* **5:** 1484–1493.

Gormanns, P., Gormanns, P., Reckow, S., Reckow, S., Poczatek, J.C., Poczatek, J.C., *et al.* (2012) Segmentation of multi-isotope imaging mass spectrometry data for semi-automatic detection of regions of interest. *PLoS ONE* **7:** e30576.

Hayes, J.M. (2001) Fractionation of carbon and hydrogen isotopes in biosynthetic processes. *Rev Mineral Geochem* **43:** 225–277.

Herrmann, A.M., Clode, P.L., Fletcher, I.R., Nunan, N., Stockdale, E.A., O'Donnell, A.G., and Murphy, D.V. (2006) A novel method for the study of the biophysical interface in soils using nano-scale secondary ion mass spectrometry. *Rapid Commun Mass Spectrom* **21:** 29–34.

Hoehler, T.M., and Jørgensen, B.B. (2013) Microbial life under extreme energy limitation. *Nat Rev Microbiol* **11:** 83–94.

Hoppe, P., Cohen, S., and Meibom, A. (2013) NanoSIMS: technical aspects and applications in cosmochemistry and biological geochemistry. *Geostand Geoanal Res* **37:** 111–154.

Katz, J.J. (1960) Chemical and biological studies with deuterium. *Am Sci* **48:** 544–580.

Kellermann, M.Y., Wegener, G., Elvert, M., Yoshinaga, M.Y., Lin, Y.-S., Holler, T., *et al*. (2012) Autotrophy as a predominant mode of carbon fixation in anaerobic methane-oxidizing microbial communities. *PNAS* **109:** 19321–19326.

Kempf, V.A., Trebesius, K., and Autenrieth, I.B. (2000) Fluorescent in situ hybridization allows rapid identification of microorganisms in blood cultures. *J Clin Microbiol* **38:** 830–838.

Koch, A.L., and Levy, H.R. (1955) Protein turnover in growing cultures of Escherichia coli. *J Biol Chem* **217:** 947–957.

Kreiswirth, B.N., Lofdahl, S., Betley, M.J., O'Reilly, M., Schlievert, P.M., Bergdoll, M.S., and Novick, R.P. (1983) The toxic shock syndrome exotoxin structural gene is not detectably transmitted by a prophage. *Nature* **305:** 709–712.

Kushner, D.J., Baker, A., and Dunstall, T.G. (1999) Pharmacological uses and perspectives of heavy water and deuterated compounds. *Can J Physiol Pharmacol* **77:** 79–88.

de Laeter, J.R., Böhlke, J.K., De Bièvre, P., Hidaka, H., Peiser, H.S., Rosman, K.J.R., and Taylor, P.D.P. (2003) Atomic weights of the elements. Review 2000 (IUPAC Technical Report). *Pure Appl Chem* **75:** 683–800.

Lechene, C.P., Hillion, F., McMahon, G., Benson, D., Kleinfeld, A.M., Kampf, J.P., *et al*. (2006) High-resolution quantitative imaging of mammalian and bacterial cells using stable isotope mass spectrometry. *J Biol* **5:** 20.

Lechene, C.P., Luyten, Y., McMahon, G., and Distel, D.L. (2007) Quantitative imaging of nitrogen fixation by individual bacteria within animal cells. *Science* **317:** 1563–1566.

Lechene, C.P., Lee, G.Y., Poczatek, J.C., Toner, M., and Biggers, J.D. (2012) 3D multi-isotope imaging mass spectrometry reveals penetration of 18O-trehalose in mouse sperm nucleus. *PLoS ONE* **7:** e42267.

Lepage, G., and Roy, C.C. (1986) Direct transesterification of all classes of lipids in a one-step reaction. *J Lipid Res* **27:** 114–120.

Lincoln, R.A., Leigh, J.A., and Jones, N.C. (1995) The amino-acid-requirements of staphylococcus-aureus isolated from cases of Bovine mastitis. *Vet Microbiol* **45:** 275–279.

Lozano, M.M., Liu, Z., Sunnick, E., Janshoff, A., Kumar, K., and Boxer, S.G. (2013) Colocalization of the ganglioside G(M1) and cholesterol detected by secondary ion mass spectrometry. *J Am Chem Soc* **135:** 5620–5630.

Mah, R.A., Fung, D.Y., and Morse, S.A. (1967) Nutritional requirements of Staphylococcus aureus S-6. *Appl Microbiol* **15:** 866–870.

Maharjan, R.P., Seeto, S., and Ferenci, T. (2007) Divergence and redundancy of transport and metabolic rate-yield strategies in a single Escherichia coli population. *J Bacteriol* **189:** 2350–2358.

Mandelstam, J. (1960) The intracellular turnover of protein and nucleic acids and its role in biochemical differentiation. *Bacteriol Rev* **24:** 289–308.

Mandelstam, J., and Halvorson, H. (1960) Turnover of protein and nucleic acid in soluble and ribosome fractions of non-growing *Escherichia coli*. *Biochim Biophys Acta* **40:** 43–49.

Marr, A.G., Nilson, E.H., and Clark, D.J. (1963) The maintenance requirement of Escherichia coli. *Ann N Y Acad Sci* **102:** 536–548.

Morono, Y., Terada, T., and Nishizawa, M. (2011) Carbon and nitrogen assimilation in deep subseafloor microbial cells. *PNAS* **108:** 18295–18300.

Musat, N., Halm, H., Winterholler, B., Hoppe, P., Peduzzi, S., Hillion, F., *et al*. (2008) A single-cell view on the ecophysiology of anaerobic phototrophic bacteria. *Proc Natl Acad Sci USA* **105:** 17861–17866.

Musat, N., Stryhanyuk, H., Bombach, P., Adrian, L., Audinot, J.-N., and Richnow, H.H. (2014) The effect of FISH and CARD-FISH on the isotopic composition of 13C- and 15N-labeled *Pseudomonas putida* cells measured by nanoSIMS. *Syst Appl Microbiol* **37:** 267–276.

Nikolic, N., Barner, T., and Ackermann, M. (2013) Analysis of fluorescent reporters indicates heterogeneity in glucose uptake and utilization in clonal bacterial populations. *BMC Microbiol* **13:** 258.

Orphan, V.J., and House, C.H. (2009) Geobiological investigations using secondary ion mass spectrometry: microanalysis of extant and paleo-microbial processes. *Geobiology* **7:** 360–372.

Orphan, V.J., Turk, K.A., Green, A.M., and House, C.H. (2009) Patterns of 15N assimilation and growth of methanotrophic ANME-2 archaea and sulfate-reducing bacteria within structured syntrophic consortia revealed by FISH-SIMS. *Environ Microbiol* **11:** 1777–1791.

Pernice, M., Meibom, A., Van Den Heuvel, A., Kopp, C., Domart-Coulon, I., Hoegh-Guldberg, O., and Dove, S. (2012) A single-cell view of ammonium assimilation in coral–dinoflagellate symbiosis. *ISME J* **6:** 1314–1324.

Pine, M.J. (1970) Steady-state measurement of the turnover of amino acid in the cellular proteins of growing Escherichia coli: existence of two kinetically distinct reactions. *J Bacteriol* **103:** 207–215.

Pine, M.J. (1972) Turnover of intracellular proteins. *Annu Rev Microbiol* **26:** 103–126.

Podolsky, R.J. (1953) Protein degradation in bacteria. *Arch Biochem Biophys* **45:** 327–340.

Polerecky, L., Adam, B., Milucka, J., Musat, N., Vagner, T., and Kuypers, M.M.M. (2012) Look@NanoSIMS – a tool for the analysis of nanoSIMS data in environmental microbiology. *Environ Microbiol* **14:** 1009–1023.

Popa, R., Weber, P.K., Pett-Ridge, J., Finzi, J.A., Fallon, S.J., Hutcheon, I.D., *et al*. (2007) Carbon and nitrogen fixation

and metabolite exchange in and between individual cells of Anabaena oscillarioides. *ISME J* **1:** 354–360.
Pratt, J.M., Petty, J., Riba-Garcia, I., Robertson, D., Gaskell, S.J., Oliver, S.G., and Beynon, R.J. (2002) Dynamics of protein turnover, a missing dimension in proteomics. *Mol Cell Proteomics* **1:** 579–591.
Rahme, L.G., Stevens, E.J., Wolfort, S.F., Shao, J., Tompkins, R.G., and Ausubel, F.M. (1995) Common virulence factors for bacterial pathogenicity in plants and animals. *Science* **268:** 1899–1902.
Rodríguez-Ruiz, J., Belarbi, E.H., Sánchez, J.L.G., and Alonso, D.L. (1998) Rapid simultaneous lipid extraction and transesterification for fatty acid analyses. *Biotechnol Tech* **12:** 689–691.
Sessions, A., and Hayes, J.M. (2005) Calculation of hydrogen isotopic fractionations in biogeochemical systems. *Geochim Cosmochim Acta* **69:** 593–597.
Sessions, A., Hayes, J.M., Sylva, S., and Summons, R. (2004) Isotopic exchange of carbon-bound hydrogen over geologic timescales. *Geochim Cosmochim Acta* **68:** 1545–1559.
Slodzian, G., Wu, T.-D., Bardin, N., Duprat, J., Engrand, C., and Guerquin-Kern, J.-L. (2014) Simultaneous hydrogen and heavier element isotopic ratio images with a scanning submicron ion probe and mass resolved polyatomic ions. *Microsc Microanal* **20:** 577–581.
Spormann, A.M., Behrens, S., Losekann, T., Pett-Ridge, J., Weber, P.K., Ng, W.-O., *et al*. (2008) Linking microbial phylogeny to metabolic activity at the single-cell level by using enhanced element labeling-catalyzed reporter deposition fluorescence in situ hybridization (EL-FISH) and NanoSIMS. *Appl Environ Microbiol* **74:** 3143–3150.
Steinhauser, M.L., and Lechene, C.P. (2013) Quantitative imaging of subcellular metabolism with stable isotopes and multi-isotope imaging mass spectrometry. *Semin Cell Dev Biol* **24:** 661–667.
Steinhauser, M.L., Bailey, A.P., Senyo, S.E., Guillermier, C., Perlstein, T.S., Gould, A.P., *et al*. (2012) Multi-isotope imaging mass spectrometry quantifies stem cell division and metabolism. *Nature* **481:** 516–519.
Thomas, A.F. (1971) Deuterium labeling in organic chemistry. New York: Appleton-Century-Crofts.
Thompson, A.W., Foster, R.A., Krupke, A., Carter, B.J., Musat, N., Vaulot, D., *et al*. (2012) Unicellular Cyanobacterium symbiotic with a single-celled Eukaryotic Alga. *Science* **337:** 1546–1550.
Urbá, R.C. (1959) Protein breakdown in *Bacillus cereus*. *Biochem J* **71:** 513–518.
Valentine, D.L. (2009) Isotopic remembrance of metabolism past. *Proc Natl Acad Sci USA* **106:** 12565–12566.
Wagner, M. (2009) Single-cell ecophysiology of microbes as revealed by Raman microspectroscopy or secondary ion mass spectrometry imaging. *Annu Rev Microbiol* **63:** 411–429.
Wegener, G., Bausch, M., Holler, T., Thang, N.M., Prieto Mollar, X., Kellermann, M.Y., *et al*. (2012) Assessing sub-seafloor microbial activity by combined stable isotope probing with deuterated water and 13C-bicarbonate. *Environ Microbiol* **14:** 1517–1527.
Wilbanks, E.G., Jaekel, U., Salman, V., Humphrey, P.T., Eisen, J.A., Facciotti, M.T., *et al*. (2014) Microscale sulfur cycling in the phototrophic pink berry consortia of the Sippewissett Salt Marsh. *Environ Microbiol* **16:** 3398–3415.
Woebken, D., Hoehler, T.M., Burow, L.C., Prufert-Bebout, L., Bebout, B.M., Pett-Ridge, J., *et al*. (2012) Identification of a novel cyanobacterial group as active diazotrophs in a coastal microbial mat using NanoSIMS analysis. *ISME J* **6:** 1427–1439.
Woebken, D., Burow, L.C., Behnam, F., Mayali, X., Schintlmeister, A., Fleming, E.D., *et al*. (2014) Revisiting N_2 fixation in Guerrero Negro intertidal microbial mats with a functional single-cell approach. *ISME J* **9:** 485–496.
Zhang, D.-S., Piazza, V., Perrin, B.J., Rzadzinska, A.K., Poczatek, J.C., Wang, M., *et al*. (2012) Multi-isotope imaging mass spectrometry reveals slow protein turnover in hair-cell stereocilia. *Nature* **481:** 520–524.
Zhang, X., Gillespie, A.L., and Sessions, A. (2009) Large D/H variations in bacterial lipids reflect central metabolic pathways. *Proc Natl Acad Sci USA* **106:** 12580–12586.
Zhang, Y.M., and Rock, C.O. (2008) Membrane lipid homeostasis in bacteria. *Nat Rev Microbiol* **6:** 222–233.

Supporting information

Additional Supporting Information may be found in the online version of this article at the publisher's web-site:

Appendix S1. Error in mass balance calculations with δ-values.
Appendix S2. Error from shot noise.
Appendix S3. Single-cell analysis in plastic.
Appendix S4. Effect of isotopic spike present during fixation.
Appendix S5. ^2H_2O toxicity.
Appendix S6. Growth rate calculations.
Appendix S7. Incubation time requirements.
Appendix S8. Log-normal growth rate distribution.
Appendix S9. Additional data tables and figures.

Appendix S1. Error in mass balance calculations with δ-values

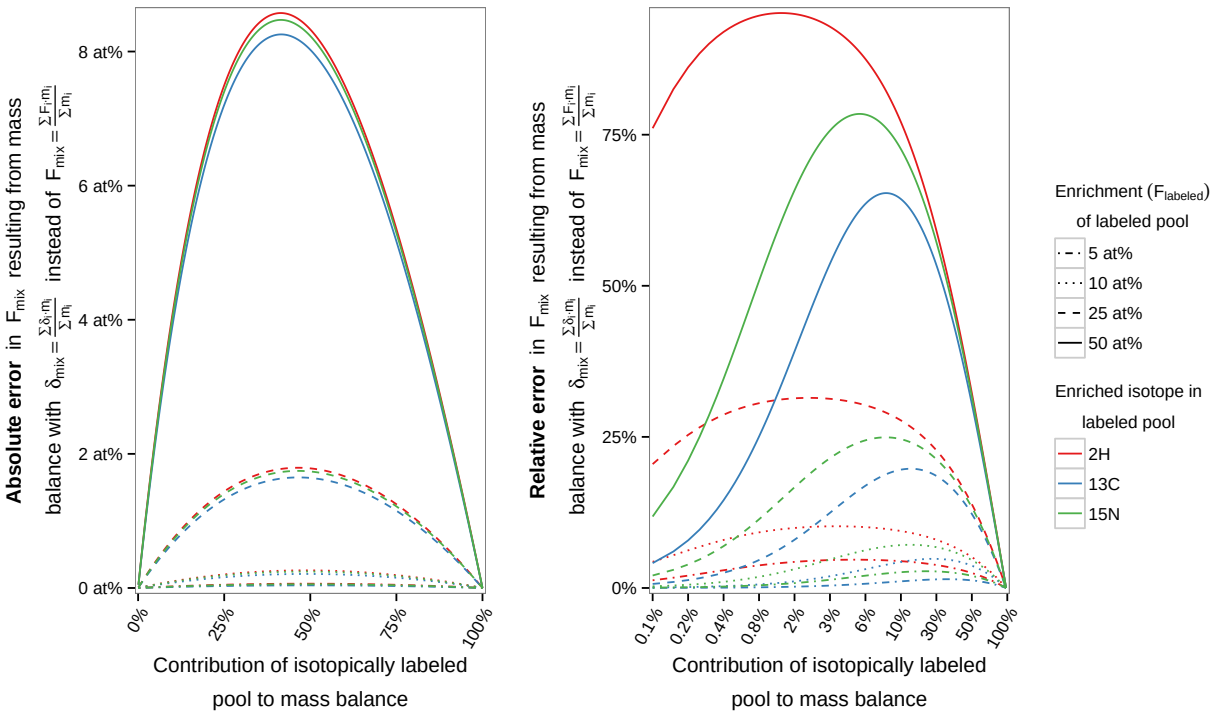

Figure S1.1: **Errors in mass balance calculations with δ-values.** Absolute (left) and relative (right) error introduced by mass balance calculations using the δ-value approximation ($\delta_{mix} \sum m_i \approx \sum \delta_i m_i$) instead of fractional abundances ($F_{mix} \sum m_i = \sum F_i m_i$). Errors introduced by the approximation are illustrated for hydrogen, carbon and nitrogen and plotted as a function of mixing between an isotopically unlabeled (natural abundance) end-member and an isotopically enriched pool (ranging in fractional abundance of the rare isotope from 5 at% to 50 at%).

Isotopic mass balance can be approximated with isotopic values in δ-notation ($\delta_{mix} \sum m_i \approx \sum \delta_i m_i$) when the isotopic composition of all pools is relatively close to natural abundance. However, this approximation introduces significant error when one or multiple pools of heavily enriched materials are part of the mass balance. This is routinely the case when working with isotopic labels and it is important to use exact mass balance calculations with fractional abundance values F instead, i.e. $F_{mix} \sum m_i = \sum F_i m_i$. Figure S1.1 illustrates the absolute and relative error introduced in the estimate of F_{mix} if mass balance between an isotopically labeled and a natural abundance (unlabeled) pool is calculated using δ-values (and then converted to F_{mix} for comparison) vs. the exact calculation in abundance space. Mass balance using δ-values systematically overestimates the true value. The error scales with the strength of the isotope label (here pictured up to a composition of $F_{labeled} = 50\%$ rare isotope in the labeled pool) and is slightly more pronounced for isotopic

systems with lower natural abundance isotope ratios (error for H > N > C). It is important to note that while the absolute error introduced from calculations with δ-values is most pronounced at a ~1:1 mixing ratio (slightly offset from 50% because natural abundances are not 0%), relative errors in the estimate for F_{mix} reach significant levels (> 10%) already with very little addition of a heavy isotope label. This aspect of δ-value mass balance limits the ability to accurately infer microbial activity in isotope labeling experiments. For this reason, fractional abundances were used for all mass balance calculations in this study.

Appendix S2. Error from shot noise

Even if detection, amplification and signal conversion in isotope ratio measurements were completely free of noise, there would still be a theoretical limit to the maximum attainable precision of isotopic data. This limit is posed by shot noise, a consequence of the discrete nature of electronic charge (whether it is carried by electrons or ions). The statistical error from shot noise is rarely a concern in standard bulk isotope measurements, but due to the low number of ions detected and limited chance for reanalysis from measuring individual cells in secondary ion mass spectrometry, this error estimate provides an important constraint on precision. This is particularly relevant in measurements of ions from low abundance elements, ions with low ionization efficiency or with rare minor isotopes (hydrogen qualifies for the last two). The error from shot noise is often considered in terms of the resulting isotope ratio or δ-value (Fitzsimons et al., 2000; Hayes, 2002), but rarely in terms of fractional abundances.

The number of ions N observed at a detector in a fixed time interval t follows a Poisson distribution (i.e., a discrete probability distribution of independent events occurring with an average rate of a). The corresponding probability mass function is $f(N) = P(X = N) = \frac{(at)^N e^{-at}}{N!}$. The expected value $E[N] = \bar{N}$ (mean) of a Poisson distribution is $\bar{N} = at$ (for a fixed time interval t). The variance $Var[N]$ of a Poisson distribution is identical to the expected value, and hence the standard deviation σ_N scales with the square root of $\bar{N}$ $\left(\sigma_N = \sqrt{Var[N]} = \sqrt{\bar{N}}\right)$. This has two important consequences for the quantification of ion currents in secondary ion mass spectrometry:

- The relative error $\frac{\sigma_N}{N} = \frac{1}{\sqrt{N}}$ decreases with higher ion counts (i.e. longer counting at constant rates makes the measurement more precise)
- There are diminishing returns due to the $\sqrt{N}^{-1}$ dependence

As a concrete example, consider an ion current of 1000 ions/s. If you repeatedly observed this ion beam for exactly 1s, you would detect 1000 ions *on average*, but with $\sigma_N = 31.6$ (or 3.16% error). If you repeatedly observed this same ion beam for 2s instead, you would detect 2000 ions on average, but with $\sigma_N = 44.7$ (or 2.24% error, a $\sqrt{2}^{-1}$ improvement). This counting error ($\sigma_N = \sqrt{N}$) is propagated readily to the resulting isotope ratios $R = \frac{i_m}{i_M}$ (m=minor,M=major isotope), fractional abundances $F = \frac{i_m}{i_M + i_m}$ and δ-values $\delta = \frac{R_1}{R_2} - 1$ by standard

error propagation. For details on σ_R and σ_δ, see Fitzsimons et al. (2000); Hayes (2001). σ_F is derived as follows:

$$\begin{aligned}
\sigma_F^2 &= \left(\frac{\partial F}{\partial N_m}\right)^2 \sigma_{N_m}^2 + \left(\frac{\partial F}{\partial N_M}\right)^2 \sigma_{N_M}^2 = \left(\frac{N_M}{(N_m+N_M)^2}\right)^2 \sigma_{N_m}^2 + \left(-\frac{N_m}{(N_m+N_M)^2}\right)^2 \sigma_{N_M}^2 \\
&= \frac{N_M^2 N_m^2}{(N_m+N_M)^4}\left[\left(\frac{\sigma_{N_m}}{N_m}\right)^2 + \left(\frac{\sigma_{N_M}}{N_M}\right)^2\right] = F^2(1-F)^2\left[\left(\frac{\sigma_{N_m}}{N_m}\right)^2 + \left(\frac{\sigma_{N_M}}{N_M}\right)^2\right] \\
&\rightarrow \left(\frac{\sigma_F}{F}\right)^2 = (1-F)^2\left(\frac{1}{N_m}+\frac{1}{N_M}\right) = \frac{(1-F)^2}{N_M F}
\end{aligned} \tag{B.1}$$

Appendix S3. Single cell analysis in plastic

Multi-isotope imaging mass spectrometry in thin section vastly expands the range of applicability of this technique to complex systems. However, many thin sectioning techniques with a relatively soft, removable matrix (e.g. embedding in OCT for cryosectioning, or embedding in paraffin) do not permit cutting sections thinner than ~5µm. While less problematic for large eukaryotic cells, this limits the potential applicability for microbial cells within larger communities or host systems where accurate targeting and identification of individual microbial cells in an ion image require even thinner sections. Hard polymerizing plastic resins developed for electron microscopy, such as LR White, provide the matrix support required for ultra-thin sections, however, they are often too dense to permit the easy use of fluorescent staining techniques important for microbial identification, such as fluorescence *in-situ* hybridization. Here, we thus use the plastic polymer Technovit, which is of intermediate hardness, and allows both routine sectioning to ~1µm thickness as well as application of most fluorescent staining techniques (Takechi et al., 1999, McGlynn et al., in prep.). Technovit works well for preserving the structure of a sample and, unlike most resins, polymerizes at cold temperatures (~4°C), precluding the need for extended exposure to relatively high heat (and the associated risk for structural changes). The structural support lent by the plastic matrix provides thin sections with a smooth surface that enables high spatial resolution in imaging mass-spectrometry due to the lack of strong topological features. However, as an acryl plastic (a combination of methyl methacrylate and glycol methacrylate), the Technovit resin contributes significant amounts of isotopically circumnatural carbon and hydrogen that dilute the isotopic signal from enriched cells. It is thus imperative to calibrate and correct any isotopic measurements of single cells embedded in plastic.

To measure embedded bacterial isotope standards, aliquots of all standards were concentrated by centrifugation, suspended in a few drops of molten noble agar (2% Difco Agar Noble in 50mM HEPES buffered filter-sterilized water), solidified by cooling at room temperature, cut into ~2mm^{3}cubes, resuspended in 50% EtOH in PBS, and dehydrated in 100% Ethanol over the course of 3 exchanges, with final resuspension in 100% for at least 1 hour. Ethanol was then replaced twice with 100% Technovit 8100 infiltration solution (Heraeus Kulzer GmbH, #64709012) to infiltrate the agar plugs over night. Agar plugs were finally suspended in airtight 0.6mL microcentrifuge tubes in Technovit 8100 infiltration solution amended with hardener II reagent and stored at 4ºC

over night to complete polymerization. Technovit is a cold-polymerizing nitrogen-free acryl plastic composed of methyl methacrylate and glycol methacrylate.

Thin sections (1-2 µm thick) were cut using a rotary microtome. Each section was stretched on the surface of a 1.5µL drop of 0.2µm filtered deionized water on a 1" diameter round microprobe slides (Lakeside city, IL) and air-dried at room temperature. The glass rounds were mapped microscopically with a 40x air objective for later orientation and sample identification during secondary ion mass spectrometry. The rounds were sputterd-coated with a 50nm layer of gold to provide a conductive surface (Dekas et al., 2009; Dekas and Orphan, 2011). Bacterial cells in the plastic sections were analyzed by NanoSIMS using a ∼1.9pA primary Cs^+ beam and were pre-sputtered with a ∼175pA primary Cs^+ beam current (I_{pre}) for 4 to 8 minutes (t), depending on the size of the pre-sputtering area (A), to a cumulative charge density of ∼350pC/µm^2 ($I_{pre} \cdot t/A$).

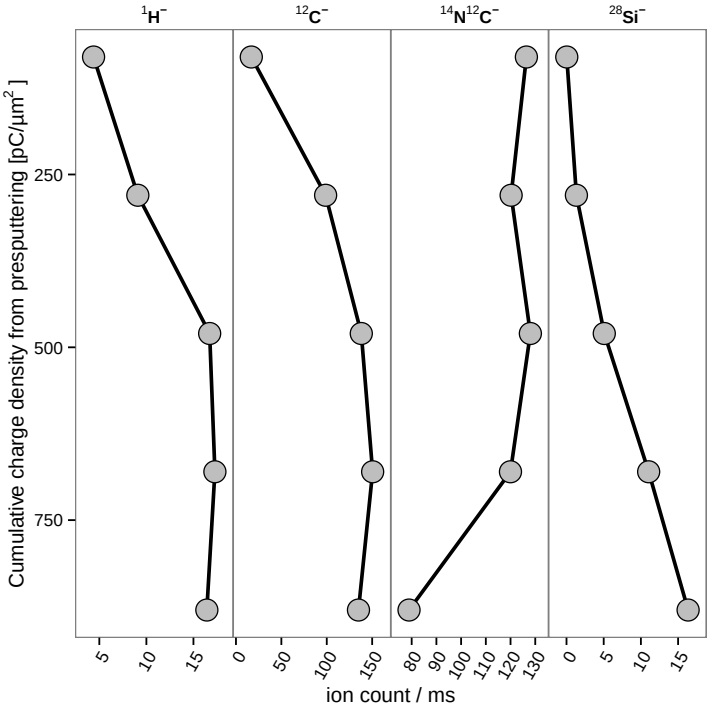

Figure S3.1: **Ionization efficiency and sample ablation in embedded cells.** Ion counts of the major H, C and N ions, as well as Si after various extents of primary ion beam exposure (quantified as cumulative charge density $I_{pre} \cdot t/A$ from pre-sputtering with primary Cs^+ beam current $I_{pre} \approx 175$ pA). Detection of $^{28}Si^-$ illustrates the gradual degradation of the plastic thin section to the point where the underlying glass support contributes increasingly to the secondary ion beam.

Figure S3.1 illustrates the change in ion counts per ms for the major isotopes' ions as a function of pre-exposing plastic-embedded cells to increasing amounts of charge from the primary ion beam. Compared to whole single cells, the plastic matrix provides a material that is much more resilient to ion bombardment, as evidenced by the significantly higher pre-sputtering flux (>10x higher) required for an increase in ionization efficiency and

sample degradation. This is partly due to the gold coating, but the primary ion beam vaporizes the thin gold layer quickly (the gold is removed by the time of the first data point in Figure S3.1), and is mostly a consequence of the plastic matrix. This figure also shows the same trends observed for whole cell analysis, namely the faster increase in ionization efficiency and subsequent quicker depletion of nitrogen. Additionally, $^{28}Si^-$ ions were collected in addition to H, C and N ions, and illustrate the gradual degradation of the plastic to the point where the underlying glass starts to contribute to the secondary ion beam.

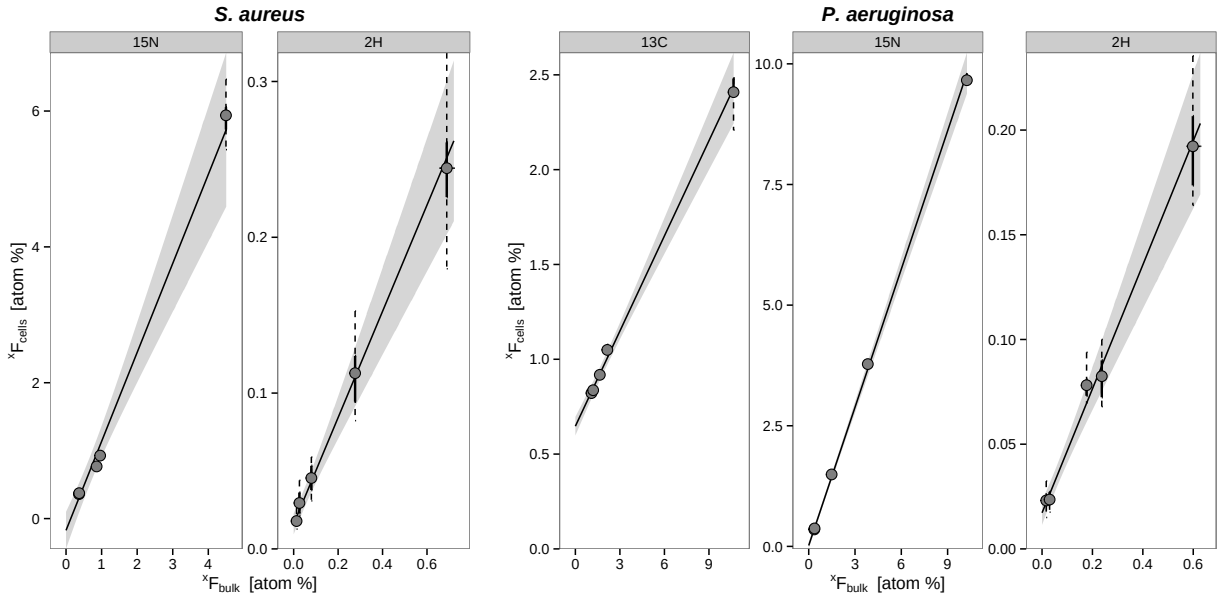

Figure S3.2: **Calibration curves for single cell vs. bulk isotope analysis.** Isotopic composition of bacterial isotope standards in embedded single cell analysis by NanoSIMS (119 ROIs for *P. aeruginosa* and 135 ROIs for *S. aureus*) vs. bulk analysis by EA-ir-MS (bulk ^{13}C and ^{15}N) and GC-pyrolysis-ir-MS (bulk fatty acid ^{2}H). All data are reported in fractional abundances ${}^xF$ (with x $=^{13}C$, ^{15}N and ^{2}H). Data points represent the mean isotopic composition of all measured single cells. The solid vertical error bars for each data point represent the range that comprises 50% of the single cell data. The dashed vertical whiskers represent the entire range of all single cell measurements. Horizontal error bars represent the total range of measured bulk isotopic composition (smaller than symbol sizes in most cases). Linear regressions are shown with 95% confidence bands.

Figure S3.2 shows the calibration curves for cells of *S. aureus* (based on 104 ROIs) and *P. aeruginosa* (based on 100 ROIs) embedded in Technovit. Table 1 provides details on all resulting calibration parameters. As expected, the nitrogen isotope compositions of embedded single cells for both organisms are not diluted by the plastic polymer (which contains no nitrogen). In *P. aeruginosa*, the calibration slope for embedded cells closely matches the slope for free whole cells (0.94 ± 0.06 and 0.95 ± 0.04), with near perfect linear correlation and slope close to 1. In the case of *S. aureus,* variability in the nitrogen isotopic composition of individual cells leads to large uncertainty observed in the calibration slope for embedded cells, which increases to 1.31 ± 0.29 and should be applied with caution.

Organism	Isotope	Calibration range ($^xF_{bulk}$ $[at\%]$)	$^xF_{cells}$ vs. $^xF_{bulk}$ slope	$^xF_{cells}$ vs. $^xF_{bulk}$ intercept $^xF[at\%]$	R^2	single cell RSD‡
P. aeruginosa	^2H	0.017 - 0.599	0.30 ± 0.06	0.0 ± 0.0	0.985	12%
S. aureus	^2H	0.013 - 0.689	0.34 ± 0.07	0.0 ± 0.0	0.981	18%
P. aeruginosa	^{13}C	1.1 - 10.7	0.17 ± 0.02	0.6 ± 0.0	0.994	1.7%
P. aeruginosa	^{15}N	0.36 - 10.25	0.95 ± 0.04	0.0 ± 0.1	0.999	0.92%
S. aureus	^{15}N	0.36 - 4.50	1.31 ± 0.29	-0.2 ± 0.3	0.981	3.1%

Table S3.1: **Calibration parameters for plastic embedded single cell vs. bulk isotope analysis.** Calibration parameters were calculated from 1/x weighted linear regression of the average isotopic composition of all single cells for a given standard vs. the measured bulk isotopic composition. Reported errors represent 95% confidence intervals from the regression.

The key observation, however, is the effect of the plastic on the carbon and hydrogen isotopic composition of the microbial isotope standards. As expected, the calibration parameters for both carbon (*P. aeruginosa* only) and hydrogen suggest substantial dilution of the isotopic signal by the plastic polymer, with the slope for carbon dropping from 0.73 ± 0.07 to 0.17 ± 0.02, and for hydrogen from 0.67 ± 0.05 to 0.30 ± 0.06 (*P. aeruginosa)* and from 0.59 ± 0.05 to 0.31 ± 0.10 (*S. aureus*). To first order, these parameters suggest a dilution of the cellular carbon by ∼75% and the cellular hydrogen by ∼50%. Although the calibration curve for carbon in embedded cells vs. bulk isotopic composition provides a robust linear correlation, the hydrogen calibration curves for both organisms suffer from elevated scatter, likely due to the same effects observed in whole cells (statistical uncertainty in the measurements for each single cell from low ion counts of ^{2}H, as well as random variation in the exact cellular components sampled by the ion beam).

These empirical relationships show that the isotopic enrichment of embedded single cells in both hydrogen and carbon (and of course nitrogen) can be quantified and used to estimate bulk isotopic compositions of individual cells in addition to measuring diversity (which can be assessed in relative terms without calibration). However, our results indicate that the high dilution of C and H by the plastic polymer restrict the accuracy of single cell isotopic measurements at relatively low levels of enrichment, and should not be used for values below $\sim 1000‰$ (i.e. 2x natural abundance). Additionally, the same caveats as for the analysis of single whole cells (extrapolation to other organisms and morphologies, statistical significance for distinguishing isotopically similar populations, etc.) equally apply. Lastly, given the relatively high scatter for these calibration curves, it is important to apply caution when using them in relating single cell isotopic compositions in plastic back to bulk equivalents.

Appendix S4. Effect of isotopic spike present during fixation

In environmental applications of isotope labeling techniques combined with microscopy and imaging mass spectrometry, cells are typically fixed with formaldehyde (or other fixatives) prior to analysis to arrest metabolism and preserve cellular structure. Frequently, fixatives are added to samples still in the presence of (some of) the isotopic label, because extensive washing procedures are either impractical (for very complex samples) or deemed

a risk to the structure and integrity of the target cells. However, fixation can both chemically and/or physically trap unincorporated isotope label that is not actually part of the cell. Such trapped isotope label is retained in excess of true cellular label incorporation, and can lead to an overestimate of microbial activity upon analysis. To estimate the potential extent of this effect, additional aliquots of cells grown without an isotopic label were fixed in the presence of the strongest employed mixture of isotope labels (1% D_2O, 10mM NH_4^+ with 10% ^{15}N, 10mM succinate with 10% ^{13}C). Table S4.1 summarizes the potential effects of the presence of a strong isotopic label during the microbial fixation with formaldehyde prior to embedding in plastic.

Microbe	Isotope	natural abundance cells $avg^x F_{cells}$ [%]	natural abundance cells σ_{x_F} [%]	spiked during fixation $avg^x F_{cells}$ [%]	spiked during fixation σ_{x_F} [%]
PA	13C	0.90	0.06	0.81	0.01
PA	15N	0.35	0.01	2.2	0.2
PA	2H	0.021	0.005	0.026	0.005
SA	15N	0.361	0.005	2.2	0.1
SA	2H	0.021	0.007	0.026	0.005

Table S4.1: **Effect of isotopic spike during fixation.** This table illustrates the effect of the presence of carbon (^{13}C succinate), hydrogen (^2H_2O) and nitrogen ($^{15}NH_4^+$) isotope labels during culture fixation with formaldehyde on the apparent isotopic composition of the microbial cells. While the presence of ^{13}C succinate and ^2H_2O does not have a significant enrichment effect within the analytical error, the presence of $^{15}NH_4$ during fixation leads to strong apparent enrichment of the microbial population that can obscure true microbial activity.

The presence of carbon (^{13}C succinate) and hydrogen (^2H_2O) does not have a significant enrichment effect within the analytical error, but the presence of $^{15}NH_4$ leads to strong apparent enrichment of the microbial population ($^{15}F \approx 2.2\%$, i.e. $\sim 5000‰$ above natural abundance). This is likely a consequence of cross-linking reactions of proteins with the isotope label and subsequent trapping of the label. The effect is considerably exaggerated here due to the nature of the experiment of mixing finely suspended single cells rapidly with both an isotope tracer and a fixating agent. Previous work on environmental samples reported less severe, but still significant abiotic ^{15}N retention of $^{15}F \approx 0.6\%$ (Orphan et al., 2009). Due to importance of sample conservation, this is often an unavoidable risk when working with a $^{15}NH_4$label. Ideally, samples are washed to remove the label prior to fixation, but whenever this is not a viable option, it is important to determine the potential extent of this effect in control experiments representative of experimental conditions.

Appendix S5. ^2H_2O toxicity

Heavy water is known to be toxic at high concentrations (Kushner et al., 1999). We tested the susceptibility of *S. aureus* to ^2H_2O by growing it in the medium used throughout this study with varying concentrations of ^2H_2O. Two growth experiments with ^2H_2O enrichments from 5% to 50% were performed at 37ºC in 96 well plates with at least 4 replicates per culture condition. Plates were shaken continuously and optical density (OD_{600nm}) was recorded every 10 minutes. Each experiment was inoculated from an overnight culture that had not previously

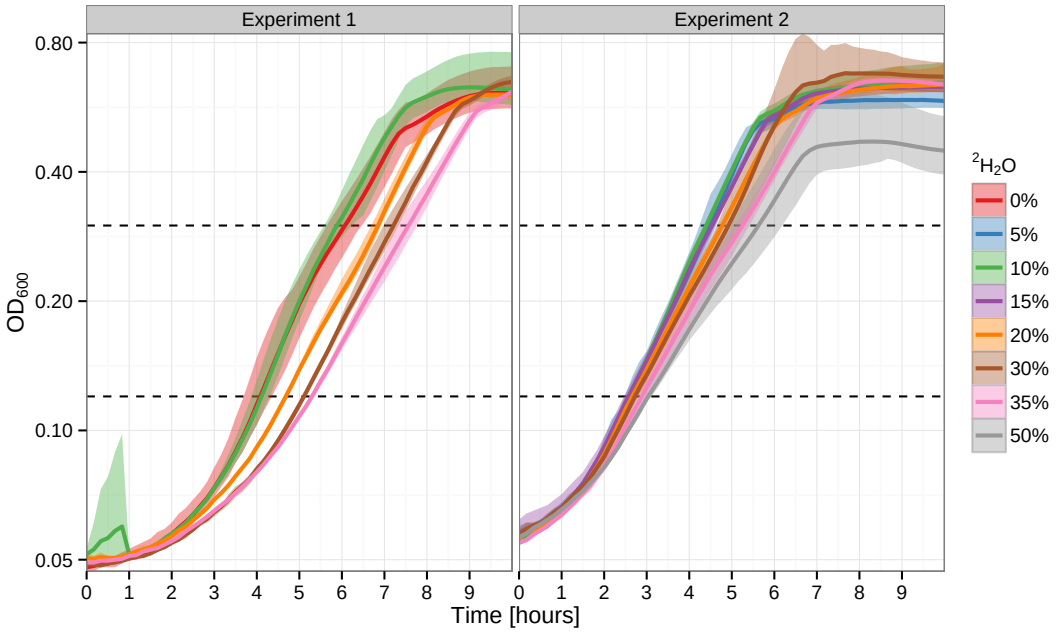

Figure S5.1: **Toxicity effects of increasing concentrations of ^2H_2O on *S. aureus*.** Semi-log growth curves of *S. aureus* in the presence of varying amounts of ^2H_2O from two separate experiments. Lines represent averages of at least 4 biological replicates, shaded area represents the maximal range of ODs in each condition. Growth rates were evaluated during mid-exponential phase (the optical density interval indicated by the dashed lines).

^2H_2O	Replicates	Mean Growth rate [1/hr]	Std. Dev.	p-value
0%	8	0.51	0.09	1.00
5%	4	0.48	0.02	0.39
10%	8	0.52	0.03	0.60
15%	4	0.47	0.01	0.27
20%	8	0.43	0.02	0.04
30%	8	0.43	0.04	0.04
35%	8	0.40	0.03	0.01
50%	4	0.36	0.06	0.01

Table S5.1: **Changes in growth rates from toxicity effects of increasing concentrations of ^2H_2O.** Summary of the observed growth rates during mid-exponential phase. Reported values are mean growth rates and standard deviation of the biological replicates for each condition. A two sample t-test was used to compare the growth rates for each experimental condition to those of the negative control (0% ^2H_2O). The resulting p-value is reported in the last column.

experienced elevated levels of ^2H_2O.

The results are summarized in Table S5.1 and indicate that in this medium, levels of ^2H_2O exposure above ~15% (i.e., 20%, 30%, 35% and 50%) caused a statistically significant ($p < 0.05$) reduction in the growth rates of *S. aureus*, that is inversely correlated with the intensity of the ^2H_2O exposure (i.e. the higher the ^2H_2O concentration, the lower the growth rate). This suggests that isotope labeling experiments with such high levels of ^2H_2O must be interpreted with caution because the label can affect the growth of *S. aureus*. Throughout this study, we employed labeling concentrations around 0.3%, well below the observed toxicity threshold of 15-20%.

Appendix S6. Growth rate calculations

The production and removal of biomass B in continuous culture is determined by the specific growth rate μ (which signifies cellular replication), turnover rate ω (which describes biosynthesis in excess of growth to compensate for degradation and turnover of proteins/lipids), and dilution rate k (which removes biomass from the culturing vessel). The set of differential equations describing the rate of change in total biomass B and the rate of change in new biomass B_{new} is the difference between the synthesis and removal fluxes:

$$\begin{aligned} \frac{dB}{dt} &= (\mu + \omega - \omega - k) \cdot B = (\mu - k) \cdot B \\ \frac{dB_{new}}{dt} &= (\mu + \omega) \cdot B - (k + \omega) \cdot B_{new} \end{aligned} \tag{F.1}$$

A differential equation for the fraction $f_{B_{new}}$ of new vs. total biomass $\left(f_{B_{new}} = \frac{B_{new}}{B}\right)$ is readily derived using the quotient rule:

$$\begin{aligned} \frac{df_{B_{new}}}{dt} &= \frac{\partial}{\partial t}\left(\frac{B_{new}}{B}\right) = \frac{1}{B}\frac{dB_{new}}{dt} - \frac{B_{new}}{B^2}\frac{dB}{dt} = \frac{1}{B}\left(\frac{dB_{new}}{dt} - f_{B_{new}}\frac{dB}{dt}\right) \\ &= (\mu + \omega) - f_{B_{new}}(k + \omega) - f_{B_{new}}(\mu - k) \\ &= (1 - f_{B_{new}}) \cdot (\mu + \omega) \end{aligned} \tag{F.2}$$

Integration provides a solution for $f_{B_{new}}(t)$ and its derivative $f'_{B_{new}}(t)$:

$$\begin{aligned} f'_{B_{new}}(t) &= (\mu + \omega) \cdot e^{-(\mu+\omega)\cdot t} \\ f_{B_{new}}(t) &= 1 - e^{-(\mu+\omega)\cdot t} \end{aligned} \tag{F.3}$$

Addition of an isotopic label with high fractional abundance F of the rare isotope x to the nutrient pool at time t_0 imparts a distinct isotopic composition ${}^xF_{B_{new}}$ on the newly produced biomass B_{new}. Isotopic mass balance between the new ($f_{B_{new}}$) and old material ($1 - f_{B_{new}}$) determines the overall isotopic composition ${}^xF_B$ of the total biomass. For time-invariant isotopic labels that lead to constant isotopic composition ${}^xF_{B_{new}}$ of all

biomass produced after addition of the isotopic spike, this yields a direct link between isotopic enrichment and growth:

$$\begin{aligned} {}^{x}F_B(t) &= {}^{x}F_{B_{new}} \cdot f_{B_{new}}(t) + {}^{x}F_B(t_0) \cdot (1 - f_{B_{new}}(t)) \\ &= ({}^{x}F_{B_{new}} - {}^{x}F_B(t_0)) \cdot \left(1 - e^{-(\mu+\omega)\cdot t}\right) + {}^{x}F_B(t_0) \end{aligned} \tag{F.4}$$

In continuous culture however, the isotopic spike is slowly diluted out of the system with dilution rate k as new medium replaces isotopically enriched substrate in the chemostat vessel, and the time-dependent isotopic composition of new biomass ${}^{x}F_{B_{new}}(t)$ has to be taken into consideration:

$${}^{x}F_B(t) = \left[\int_0^t {}^{x}F_{B_{new}}(t) \cdot f'_{B_{new}}(t) \cdot dt\right] + {}^{x}F_B(t_0) \cdot (1 - f_{B_{new}}(t)) \tag{F.5}$$

The exact isotopic composition of new biomass and corresponding solution to equation F.5 depends on the nature of the isotopic label (^{2}H from H_2O / ^{15}N from NH_4^+) and is discussed in detail for each label.

^{2}H from H_2O

In this study, the isotopic enrichment of ^{2}H resulting from growth of *S. aureus* in the presence of isotopically spiked water is traced by measuring the isotopic composition of the non-exchangeable hydrogen bound in membrane fatty acids (${}^2F_{fa}$). The isotopic composition of newly synthesized fatty acids (${}^2F_{fa_{new}}$) after administration of the isotopic spike depends (1) on the isotopic composition of the enriched medium water (${}^2F_{water}$) and (2) on the physiology of hydrogen assimilation from water.

(1) The water isotopic composition of the enriched medium is a function of the initial composition of the spiked medium (${}^2F_{spiked}$), and the dilution with fresh medium of original water isotopic composition (${}^2F_{water}(t_0)$) at dilution rate k:

$${}^{2}F_{water}(t) = {}^{2}F_{spiked} \cdot e^{-k\cdot t} + {}^{2}F_{water}(t_0)\left(1 - e^{-k\cdot t}\right) \tag{F.6}$$

(2) The isotopic composition of newly synthesized fatty acids can be considered in terms of the combination of the mole fraction of water derived hydrogen x_w and associated net hydrogen isotope fraction $\alpha_{fa/w}$, and substrate derived hydrogen ($x_w - 1$) including metabolic water (Kreuzer-Martin et al., 2006) with average substrate isotopic composition ${}^2F_{sub}$ and associated net isotope fractionation $\alpha_{fa/s}$(Sessions and Hayes, 2005; Zhang et al., 2009; Valentine, 2009):

$${}^{2}F_{fa_{new}}(t) = x_w \cdot \alpha_{fa/w} \cdot {}^{2}F_{water}(t) + (1 - x_w) \cdot \alpha_{fa/s} \cdot {}^{2}F_{sub} \tag{F.7}$$

For growth in similar medium, the physiological parameters of hydrogen assimilation (x_w, $\alpha_{fa/w}$, $\alpha_{fa/s}$) are assumed to be constant. The appropriate value of the combined water hydrogen assimilation constant

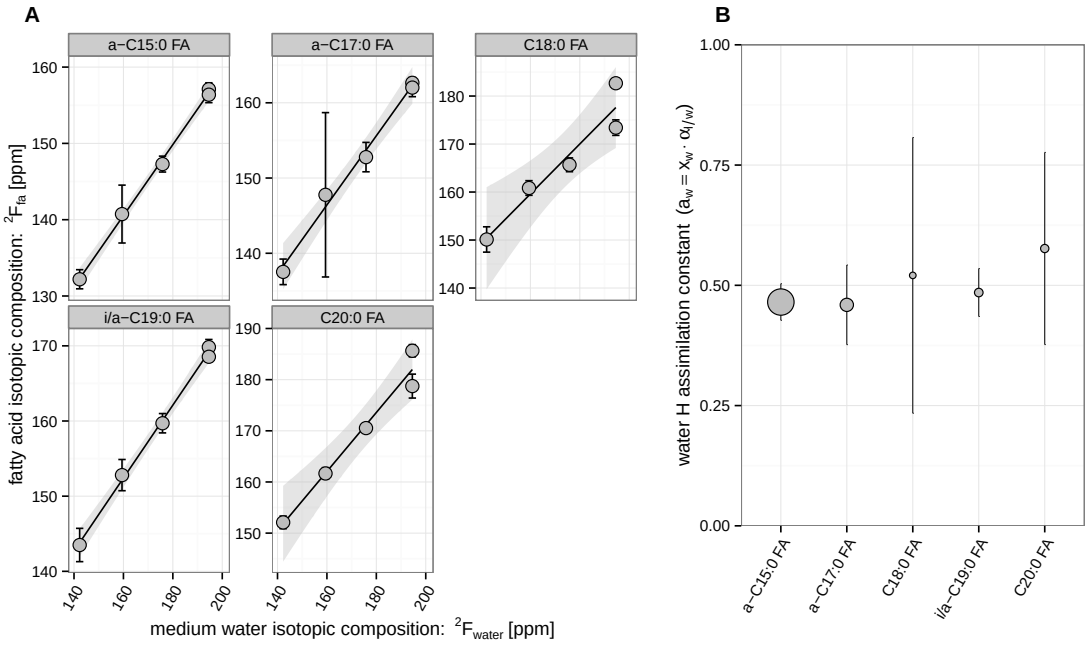

Figure S6.1: **Physiological parameters of water hydrogen assimilation for *S. aureus* growing in study medium**. **A**: Regression lines of $^2F_{fa}$ vs $^2F_{water}$ for individual fatty acids. Error bars on individual data points indicate 95% confidence intervals from up to four analytical replicates. Linear regressions are shown with 95% confidence bands. Some rare fatty acids could not be quantified in all runs. Data points without any error bars are derived from a single analysis. **B**: Summary of the water hydrogen assimilation constants (a_w) derived for individual fatty acids from regression analysis of A. Size of symbols indicates the relative membrane abundance of the individual fatty acids. Error bars indicate 95% confidence intervals of the coefficients from the linear regression fit.

Compound	% Membrane	water H assimilation constant(a_w)	R^2
a-C15:0 FA	46.7	0.47 ± 0.04	0.998
a-C17:0 FA	20.2	0.46 ± 0.08	0.990
C18:0 FA	6.7	0.52 ± 0.29	0.918
i/a-C19:0 FA	10.7	0.49 ± 0.05	0.997
C20:0 FA	10.1	0.58 ± 0.20	0.966

Table S6.1: **Water hydrogen assimilation constants for *S. aureus* growing in study medium**. Summary of the water hydrogen assimilation constants (a_w) of all major fatty acids (>5% relative abundance). Errors represent 95% confidence intervals of the coefficients from the linear regression fit.

$a_w = x_w \cdot \alpha_{fa/w}$ for *S. aureus* growing in the medium used in this study was determined following the approach of Zhang et al. (2009). Briefly, *S. aureus* was grown in batch culture experiments with four different water isotopic compositions and a_w was determined for all major membrane fatty acids from the slopes of $^2F_{fa}$ vs. $^2F_{water}$ (Figure S6.1 and Table S6.1). For calculations involving bulk fatty acid hydrogen isotope compositions, an average value for a_w (average $a_w = 0.48$) was determined from all fatty acids' a_w-values weighted by the relative abundances of the individual fatty acids. The $^2F_{sub}$-dependent contribution to fatty acid hydrogen $((1 - x_w) \cdot$

$\alpha_{fa/s} \cdot {}^2F_{sub}$) was determined from a_w and the water and fatty acid isotopic compositions in each continuous culture experiment prior to the addition of isotope tracers ($(1-x_w)\cdot\alpha_{fa/s}\cdot{}^2F_{sub} = {}^2F_{fa}(t_0) - a_w\cdot{}^2F_{water}(t_0)$). Equation F.7 thus becomes:

$$\begin{aligned} {}^2F_{fa_{new}}(t) &= a_w \cdot \left({}^2F_{water}(t) - {}^2F_{water}(t_0)\right) + {}^2F_{fa}(t_0) \\ &= a_w \cdot \left({}^2F_{spiked} - {}^2F_{water}(t_0)\right) \cdot e^{-k\cdot t} + {}^2F_{fa}(t_0) \end{aligned} \tag{F.8}$$

Substitution into equation F.5 finally yields the following solution, which is simplified by replacing the biosynthetic rates μ (cellular replication) and ω_{fa} (turnover; here for fatty acids) with the combined total growth activity rate $\mu_{act} = \mu + \omega_{fa}$ representing the overall rate of biosynthesis:

$$\begin{aligned} {}^2F_{fa}(t) &= \int_0^t {}^2F_{fa_{new}}(t) \cdot f'_{B_{new}}(t) \cdot dt \; + \; {}^2F_{fa}(t_0) \cdot (1 - f_{B_{new}}(t)) \\ &= \int_0^t a_w \cdot \left({}^2F_{spiked} - {}^2F_{water}(t_0)\right) \cdot \mu_{act} \cdot e^{-(\mu_{act}+k)\cdot t} \cdot dt \\ &\quad + \int_0^t {}^2F_{fa}(t_0) \cdot \mu_{act} \cdot e^{-\mu_{act}\cdot t} \cdot dt \; + \; {}^2F_{fa}(t_0) \cdot e^{-\mu_{act}\cdot t} \\ &= a_w \cdot \left({}^2F_{spiked} - {}^2F_{water}(t_0)\right) \cdot \frac{\mu_{act}}{\mu_{act}+k} \cdot \left(1 - e^{-(\mu_{act}+k)\cdot t}\right) + {}^2F_{fa}(t_0) \end{aligned} \tag{F.9}$$

In continuous culture at steady state, the dilution rate k sets the average growth rate of the population ($\frac{dB}{dt} = 0 \Rightarrow \bar{\mu} = k$). Here, using equation F.9, the growth activity rate μ_{act} was calculated on a *single cell* basis from NanoSIMS hydrogen isotope measurements. For each continuous culture experiment, the dilution rate k was set by the experimental setup, water isotopic compositions ${}^2F_{spiked}$ and ${}^2F_{water}(t_0)$ were measured as described in the Experimental Procedures, and bulk membrane fatty acid isotopic compositions ${}^2F_{fa}(t)$ and ${}^2F_{fa}(t_0)$ were determined from single cell hydrogen isotope measurements using the calibrations discussed in the main text.

^{15}N from NH_4^+

The isotopic enrichment of ^{15}N resulting from growth of *S. aureus* in the presence of isotopically spiked ammonium is traced by measuring the bulk nitrogen isotopic composition (${}^{15}F_{bulk}$) of single cells. Like ^{2}H from H_2O, the isotopic composition of newly synthesized biomass (${}^{15}F_{new}$) after administration of the isotopic spike depends (1) on the isotopic composition of the enriched ammonium (${}^{15}F_{NH_4^+}$) and (2) on the physiology of nitrogen assimilation.

(1) The nitrogen isotopic composition of the enriched ammonium in the medium is a function of the initial concentration and composition of ammonium in the spiked medium ($[NH_4^+]_{spiked}$ and ${}^{15}F_{spiked}$), and the dilution with fresh medium back towards the steady-state equilibrium concentration ($[NH_4^+]_{eq}$) and natural isotopic

composition ($^{15}F_{nat}$) at dilution rate k:

$$^{15}F_{NH_4^+}(t) = \frac{[\mathsf{NH_4^+}]_{spiked} \cdot {}^{15}F_{spiked} \cdot e^{-k \cdot t} + [\mathsf{NH_4^+}]_{eq} \cdot {}^{15}F_{nat} \cdot \left(1 - e^{-k \cdot t}\right)}{[\mathsf{NH_4^+}]_{spiked} \cdot e^{-k \cdot t} + [\mathsf{NH_4^+}]_{eq} \cdot (1 - e^{-k \cdot t})} \tag{F.10}$$

(2) The nitrogen isotope composition of newly synthesized biomass ($^{15}F_{new}$) depends on the relative contribution of cellular nitrogen assimilated from ammonium ($x_{NH_4^+}$) vs. all other nitrogen sources ($1 - x_{NH_4^+}$). It is important to note that it does not matter whether the steady-state pool of ammonium present at the time of spiking is composed only of the initial pool of ammonium added to the medium, or whether it contains any additional ammonium released by potential spontaneous decomposition of amino acids, assuming that both sources reflect a natural abundance isotope composition ($^{15}F_{nat}$). All nitrogen assimilated from the ammonium pool after addition of the isotopically enriched spike is isotopically distinct with composition $^{15}F_{NH_4^+}(t)$ whereas nitrogen assimilated from all other nitrogen sources (amino acids present in the culture medium) continues to reflect a natural abundance isotope composition ($^{15}F_{nat}$). The isotopic composition of cellular nitrogen derived from all natural abundance materials (unlabeled ammonium and amino acids) is assumed to be invariant and reflected in the cellular nitrogen isotope value prior to isotope labeling ($^{15}F_{bulk}(t_0) = {}^{15}F_{nat}$). Isotope fractionation associated with nitrogen assimilation from ammonium is assumed to be negligible ($^{15}\alpha \approx 1$) in the context of isotope labeling with highly enriched ^{15}N.

$$^{15}F_{new}(t) = x_{NH_4^+} \cdot {}^{15}F_{NH_4^+}(t) + \left(1 - x_{NH_4^+}\right) \cdot {}^{15}F_{bulk}(t_0) \tag{F.11}$$

Substituting equations F.10 and F.11 into equation F.5 yields:

$$\begin{aligned}
^{15}F_{bulk}(t) &= \int_0^t {}^{15}F_{new}(t) \cdot f'_{B_{new}}(t) \cdot dt \; + \; {}^{15}F_{bulk}(t_0) \cdot (1 - f_{B_{new}}(t)) \\
&= x_{NH_4^+} \cdot \int_0^t \left({}^{15}F_{NH_4^+}(t) - {}^{15}F_{bulk}(t_0)\right) \cdot (\mu + \omega_N) \cdot e^{-(\mu+\omega_N)\cdot t} \cdot dt \\
&\quad + \int_0^t {}^{15}F_{bulk}(t_0) \cdot (\mu + \omega_N) \cdot e^{-(\mu+\omega_N)\cdot t} \cdot dt \; + \; {}^{15}F_{bulk}(t_0) \cdot e^{-(\mu+\omega_N)\cdot t} \\
&= x_{NH_4^+} \cdot \int_0^t \left(\frac{[\mathsf{NH_4^+}]_{spiked} \cdot {}^{15}F_{spiked} + [\mathsf{NH_4^+}]_{eq} \cdot {}^{15}F_{bulk}(t_0) \cdot \left(e^{k \cdot t} - 1\right)}{[\mathsf{NH_4^+}]_{spiked} + [\mathsf{NH_4^+}]_{eq} \cdot (e^{k \cdot t} - 1)} - \right. \\
&\qquad \left. - {}^{15}F_{bulk}(t_0) \right) \cdot (\mu + \omega_N) \cdot e^{-(\mu+\omega_N)\cdot t} \cdot dt \; + \; {}^{15}F_{bulk}(t_0)
\end{aligned} \tag{F.12}$$

For each continuous culture experiment, the fraction of nitrogen assimilated from ammonium $x_{NH_4^+}$ was estimated on a single cell basis by numerical integration of equation F.12 with k set by the experimental setup and single cell growth rates derived from corresponding hydrogen isotope measurements (equation F.9). It is important to note that hydrogen derived growth rates μ_{act} include a component of fatty acid turnover ω_{fa}

that is unlikely to be representative of cellular nitrogen turnover ω_N. To account for this difference, hydrogen derived measurements of μ_{act} were scaled to the known average growth rate in each experiment ($\bar{\mu} = k$) to provide estimates of single cell μ, and nitrogen turnover was estimated from prior work on protein turnover ($\omega_N = 0.0275\,\mathrm{hr}^{-1}$, Pine (1970, 1972)) as discussed in the text. Ammonium concentrations $[\mathrm{NH_4^+}]_{spiked}$ and $[\mathrm{NH_4^+}]_{eq}$ were measured as described in the Experimental Procedures, and the isotopic compositions ${}^{15}F_{bulk}(t)$ and ${}^{15}F_{bulk}(t_0)$ were calculated from single cell nitrogen isotope measurements.

Appendix S7. Incubation time requirements

The incubation time requirements illustrated in Figure 1 are estimated for a given heavy water isotopic spike ${}^2F_{spiked}$ and population generation time T as follows. Assuming that the isotopic label is not diluted out of the system ($k = 0$), Equation F.9 simplifies to

$$ {}^2F_{fa}(t) = a_w \cdot \left({}^2F_{spiked} - {}^2F_{water}(t_0)\right) \cdot \left(1 - e^{-\mu \cdot t}\right) + {}^2F_{fa}(t_0) \tag{G.1} $$

Substituting the generation time for the growth rate $\left(\mu = \frac{\ln 2}{T}\right)$, and solving for the time t_{label} required to reach a final isotopic enrichment of ${}^2F_{fa}(t_{label}) = {}^2F_{final}$ yields

$$ t_{label} = \frac{T}{\ln 2} \cdot \ln\left(\frac{a_w \cdot \left({}^2F_{spiked} - {}^2F_{water}(t_0)\right)}{a_w \cdot ({}^2F_{spiked} - {}^2F_{water}(t_0)) - ({}^2F_{final} - {}^2F_{fa}(t_0))}\right) \tag{G.2} $$

with water and fatty acid isotopic compositions before spiking (at t_0) approximated by natural abundance hydrogen isotope values $\left({}^2F_{water}(t_0) = {}^2F_{fa}(t_0) = {}^2F_{nat} = 0.015574\,\mathrm{at\%}\right)$. For the purpose of this minimum incubation time estimate, the water hydrogen assimilation constant a_w was set to 0.49, a conservative estimate based on the average values of a_w measured for complex media in this study and in Zhang and Rock (2008). Higher values of a_w, such as those measured for heterotrophic growth conditions with TCA cycle intermediates as sole carbon sources, and for autotrophic metabolisms (e.g., Zhang and Rock, 2008), would always lead to *shorter* incubation time requirements.

Appendix S8. Log-normal growth rate distribution

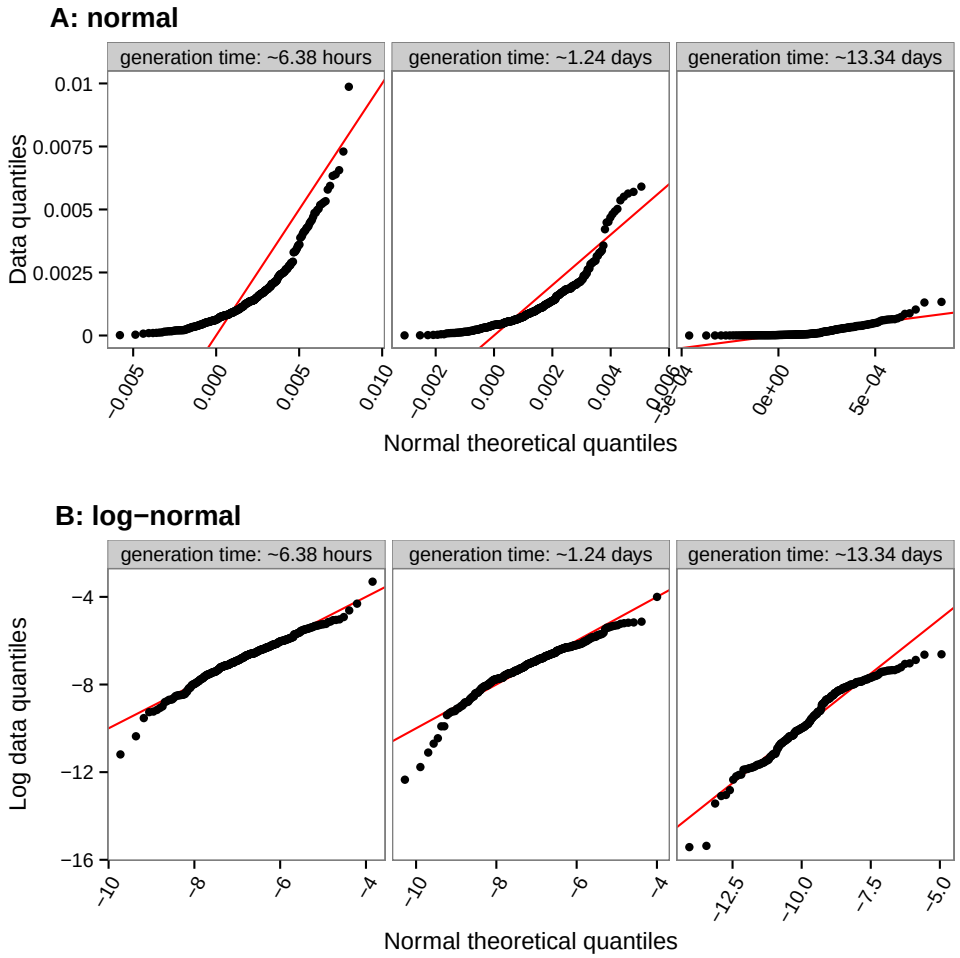

Figure S8.1: **Single cell growth rates fit log-normal distribution.** Quantile plots of the measured single cell growth rates vs. theoretical distributions show that the data is described more accurately by a log-normal (**B**) rather than a normal distribution (**A**).

Appendix S9. Additional data tables and figures

Organism	${}^{2}H\,F_{fa}$ [%]	${}^{15}N\,F_{bulk}$ [%]	${}^{13}C\,F_{bulk}$ [%]
P. aeruginosa	0.017 ± 0.000	0.360 ± 0.003	1.084 ± 0.001
P. aeruginosa	0.030 ± 0.001	0.378 ± 0.002	1.198 ± 0.007
P. aeruginosa	0.177 ± 0.006	1.485 ± 0.007	1.646 ± 0.001
P. aeruginosa	0.237 ± 0.006	3.828 ± 0.044	2.152 ± 0.007
P. aeruginosa	0.599 ± 0.042	10.247 ± 0.120	10.657 ± 0.102
S. aureus	0.013 ± 0.000	0.364 ± 0.005	
S. aureus	0.026 ± 0.000	0.369 ± 0.004	
S. aureus	0.080 ± 0.002	0.860 ± 0.029	
S. aureus	0.276 ± 0.011	0.959 ± 0.001	
S. aureus	0.689 ± 0.056	4.496 ± 0.098	

Table S9.1: **Bulk isotopic composition of microbial NanoSIMS standards.** Standards are from single pure cultures harvested in mid-exponential phase. Reported bulk hydrogen isotope compositions represent the mass balance weighted average isotopic composition of the whole membrane from all major fatty acid components. Reported errors represent 95% confidence intervals from replicate analyses.

Continuous culture generation time	Time after addition of isotopic spike	${}^{2}H\,F_{fa}$ [%]
6.38 hours	0 seconds	0.0133 ± 0.0009
6.38 hours	10 minutes	0.0152 ± 0.0003
6.38 hours	20 minutes	0.0174 ± 0.0010
6.38 hours	30 minutes	0.0191 ± 0.0003
6.38 hours	40 minutes	0.0207 ± 0.0008
6.38 hours	50 minutes	0.0231 ± 0.0020
6.38 hours	1 hours	0.0250 ± 0.0019
1.24 days	0 seconds	0.0143 ± 0.0002
1.24 days	40 minutes	0.0160 ± 0.0004
1.24 days	1.37 hours	0.0182 ± 0.0004
1.24 days	2 hours	0.0199 ± 0.0004
1.24 days	2.67 hours	0.0222 ± 0.0008
1.24 days	3.33 hours	0.0239 ± 0.0012
13.34 days	0 seconds	0.0144 ± 0.0002
13.34 days	5 hours	0.0166 ± 0.0002
13.34 days	10 hours	0.0191 ± 0.0004
13.34 days	15 hours	0.0215 ± 0.0006
13.34 days	20 hours	0.0239 ± 0.0009
13.34 days	1.04 days	0.0268 ± 0.0010
13.34 days	1.25 days	0.0303 ± 0.0012

Table S9.2: **Bulk isotopic composition of isotopically labeled cells in continuous culture.** Reported bulk hydrogen isotope compositions represent the mass balance weighted average isotopic composition of the whole membrane from all major fatty acid components. Reported errors represent 95% confidence intervals from replicate analyses.

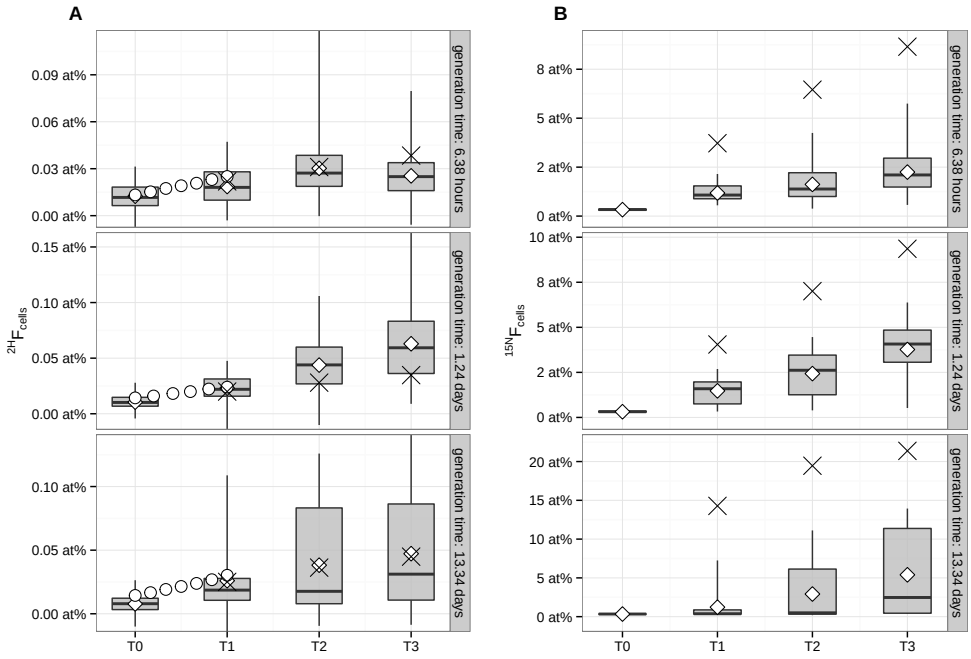

Figure S9.1: **Single cell isotopic compositions.** The three panels show the single cell data from continuous culture experiments at different growth rates. All single cell data is corrected to reflect the corresponding bulk fatty acid composition for ^{2}H (**A**) and bulk cell composition for ^{15}N (**B**) using the calibrations described in the text. The gray bands for each time point represent the range that comprises 50% of the single cell data. The whiskers represent the entire range of all single cells (upper and lower quartile). White diamonds represent the average isotopic composition of all measured single cells at a time point, and the black lines represent the median. Differences between the mean and the median reflect a skewed distribution in the isotopic composition of individual cells that is discussed in detail in the text. The white circles show the bulk membrane fatty acid hydrogen isotopic compositions (data from Table S9.2). The crosses represent the theoretically expected average isotopic composition at each time point, assuming no fatty acid turnover (^{2}H enrichment in **A**), and nitrogen turnover on the order of ω_N=2.75%/hr (as discussed in the text) with ammonium as the only source of nitrogen used by the cells (^{15}N enrichment in **B**). The substantial overestimate of the theoretical prediction for ^{15}N enrichment highlights the importance of alternative, unlabelled nitrogen sources for the cells (here, amino acids supplied in the medium), as discussed in the text.